

An integrated workflow for stress and flow modelling using outcrop-derived discrete fracture networks

Bisdom, K.; Nick, H. M.; Bertotti, G.

DOI

[10.1016/j.cageo.2017.02.019](https://doi.org/10.1016/j.cageo.2017.02.019)

Publication date

2017

Document Version

Accepted author manuscript

Published in

Computers & Geosciences: an international journal

Citation (APA)

Bisdom, K., Nick, H. M., & Bertotti, G. (2017). An integrated workflow for stress and flow modelling using outcrop-derived discrete fracture networks. *Computers & Geosciences: an international journal*, 103, 21-35. <https://doi.org/10.1016/j.cageo.2017.02.019>

Important note

To cite this publication, please use the final published version (if applicable). Please check the document version above.

Copyright

Other than for strictly personal use, it is not permitted to download, forward or distribute the text or part of it, without the consent of the author(s) and/or copyright holder(s), unless the work is under an open content license such as Creative Commons.

Takedown policy

Please contact us and provide details if you believe this document breaches copyrights. We will remove access to the work immediately and investigate your claim.

6
7

8 An integrated workflow for stress and flow 9 modelling **using outcrop-derived discrete** 10 **fracture networks**

11 K. Bisdom¹, H. M. Nick^{1,2}, G. Bertotti¹

12 1) Department of Geoscience & Engineering, Delft University of Technology, Delft,
13 Netherlands

14 2) The Danish Hydrocarbon Research and Technology Centre, Technical University of
15 Denmark, Copenhagen, Denmark

16 Keywords: permeability tensor; discrete fracture matrix; aperture; fracture permeability;
17 fracture networks; fracture mechanics; outcrop analogue modelling; Brazil

18 **Abstract**

19 Fluid flow in naturally fractured reservoirs is often controlled by subseismic-scale fracture
20 networks. Although the fracture network can be partly sampled in the direct vicinity of wells,
21 the inter-well scale network is poorly constrained in fractured reservoir models. Outcrop
22 analogues can provide data for population of domains of the reservoir model where no direct
23 measurements are available. However, extracting relevant statistics from large outcrops
24 representative of inter-well scale fracture networks remains challenging. Recent advances in
25 outcrop imaging provide high-resolution datasets that can cover areas of several hundred by
26 several hundred meters, i.e. the domain between adjacent wells, but even then, data from the

27 high-resolution models is often upscaled to reservoir flow grids, resulting in loss of accuracy.
28 We present a workflow that uses photorealistic georeferenced outcrop models to construct
29 geomechanical and fluid flow models containing thousands of discrete fractures covering
30 sufficiently large areas, that does not require upscaling to model permeability. This workflow
31 seamlessly integrates geomechanical Finite Element models with flow models that take into
32 account stress-sensitive fracture permeability and matrix flow to determine the full
33 permeability tensor. The applicability of this workflow is illustrated using an outcropping
34 carbonate pavement in the Potiguar basin in Brazil, from which 1082 fractures are digitised.
35 The permeability tensor for a range of matrix permeabilities shows that conventional
36 upscaling to effective grid properties leads to potential underestimation of the true
37 permeability and the orientation of principal permeabilities. **The presented workflow yields**
38 **the full permeability tensor model of discrete fracture networks with stress-induced apertures,**
39 **instead of relying on effective properties as most conventional flow models do.**

40 **1. Introduction**

41 Natural fracture networks are multiscale systems that develop through a combination of
42 mechanisms that are only partly understood (Olson et al., 2009; Philip et al., 2005).
43 Understanding the multiscale distribution of fracture networks in the subsurface allows for
44 optimisation of fractured reservoir development (Nelson, 2001). **However, limited**
45 **observations from seismic and wells do not provide the complete fracture network geometry**
46 **and associated flow properties, particularly of the subseismic fracture network** (Fabuel-Perez
47 et al., 2010; **Martinez-Landa et al., 2016**). Outcrops are the only source to obtain realistic
48 descriptions of fracture networks, as no models exist that can create realistic fracture
49 networks on the scale of fractured reservoirs. To derive lessons for fractured reservoirs, we
50 need outcropping datasets that contain at least several hundred fractures covering several
51 orders of magnitude in spacing and length, without suffering from censoring and truncation

52 artefacts, over an area that covers at least several grid blocks in conventional reservoir flow
53 models (Bonnet et al., 2001; Ortega et al., 2006). Such datasets are not easily obtained from
54 conventional outcrop photographs or scanline studies, as these methods capture only a limited
55 number of scales (Bisdorn et al., 2014).

56 Photogrammetry, particularly Structure from Motion (SfM) Multiview stereo (MVS),
57 is an inexpensive and fast method to accurately map 3-D structures from 2-D images taken
58 from different positions (Harwin and Lucieer, 2012; Ullman, 1979). In recent years, this
59 method has been embraced by geologists to create digital outcrop models as an alternative to
60 the more expensive and less flexible LiDAR (Light Image Detection And Ranging) methods
61 (Hodgetts, 2013; Mahmud et al., 2015; Reif et al., 2011; Rotevatn et al., 2009; Tavani et al.,
62 2014; Wilson et al., 2011). Partly overlapping images are aligned by identifying and
63 extracting common points, which can be positioned in 3-D space to reconstruct the outcrop
64 geometry (Bemis et al., 2014; James and Robson, 2012). The resulting models provide a
65 complete and unobstructed viewpoint of the outcrop that can be changed and adjusted for any
66 purpose (Tavani et al., 2016).

67 As this approach requires that the outcrop is fully covered by images with an overlap
68 of at least 50%, Unmanned Aerial Vehicles (UAVs or drones), equipped with a camera and
69 positioning sensors, are best suited to acquire the images required for photogrammetry
70 modelling (e.g. Bemis et al., 2014; Bond et al., 2015; Hodgetts, 2013; James and Robson,
71 2012; Tavani et al., 2014; Vasuki et al., 2014; Vollgger and Cruden, 2016). Fracture
72 geometries can be extracted from the resulting georeferenced models in 2-D or 3-D (Duelis
73 Viana et al., 2016; Hardebol and Bertotti, 2013; Tavani et al., 2014). Extraction of 2-D data
74 from a 3-D photogrammetry model is more accurate than fracture interpretation from
75 conventional 2-D images, as the photogrammetry model is accurately orthorectified and the
76 multiple viewpoints allow for more precise digitisation of fracture geometry. Irrespective of

77 whether the fracture data is used for 2-D or 3-D analysis, 3-D outcrop models provide a
78 higher accuracy.

79 The second challenge is to obtain realistic aperture predictions from outcropping
80 geometries. At depth, permeability is a function of aperture, which is partly controlled by the
81 in-situ stresses (Baghbanan and Jing, 2008; Lei et al., 2015; Tao et al., 2009; Zoback, 2007),
82 but pressure relief during exhumation and weathering dissolves cements and changes
83 aperture. Outcropping apertures are therefore not representative, unless it can be proven that
84 fractures have not been reactivated during exhumation. This is typically assumed to be the
85 case for veins (e.g. Hooker et al., 2014), but preserved veins are relatively rare. Alternatively,
86 aperture is modelled as a function of stress, using subcritical crack growth as defined by
87 Linear Elastic Fracture Mechanics (LEFM) or conductive shearing defined by Barton-Bandis
88 (Barton, 1982; Barton et al., 1985; Barton and Bandis, 1980; Lawn and Wilshaw, 1975;
89 Olson, 2003; Pollard and Segall, 1987; Vermilye and Scholz, 1995). These models require
90 the local stress state, which is typically derived from Finite Element (FE) models with
91 explicit fracture representations (Barton, 2014; Bisdorn et al., 2016b; Lei et al., 2016, 2014;
92 Nick et al., 2011).

93 The third challenge is modelling permeability through fractured rocks, taking into
94 account the coupled flow through fractures and matrix (Belayneh et al., 2009; Geiger et al.,
95 2013; Lang et al., 2014). Conventional reservoir simulation tools scale up fracture density,
96 porosity and permeability to effective grid properties in dual-porosity dual-permeability
97 grids, resulting in a significantly simplified flow model (Cottureau et al., 2010; Geiger and
98 Matthäi, 2012; Jonoud and Jackson, 2008). Methods exist to model flow through discrete
99 fracture-matrix models without requiring upscaling, making use of a Finite-Element Finite-
100 Volume (FE-FV) approach, but the use of these methods is often limited to relatively small-
101 scale synthetic fracture networks (Lei et al., 2014; Matthäi and Belayneh, 2004).

102 These individual problems have been studied extensively, focusing on 3-D outcrop
103 modelling (Hodgetts, 2013; Tavani et al., 2014; Vasuki et al., 2014), meshing (Karimi-Fard
104 and Durlofsky, 2016; Nejati et al., 2016; Nick and Matthäi, 2011a; Paluszny et al., 2007) and
105 flow modelling (Lang et al., 2014; Nick and Matthäi, 2011b), but integrating these
106 components remains a challenge. Our aim is to present an integrated workflow for modelling
107 the complete permeability tensor of large-scale fracture networks with apertures
108 representative of in-situ stress conditions by combining fast data acquisition using a UAV
109 with outcrop modelling using photogrammetry (Figure 1). This workflow builds upon the
110 stress-aperture modelling approach presented in Bisdorn et al. (2016b), making use of the
111 geometrical aperture approximation from Bisdorn et al. (2016d), and the modelling of
112 permeability for a range of aperture definitions presented in (Bisdorn et al., 2016d). The 3-D
113 outcrop models are used to accurately digitise fracture patterns in 2-D, which form the basis
114 for stress, aperture and equivalent permeability (i.e. combined matrix and fracture
115 permeability) models. The main result is a discrete fracture-matrix model consisting of an
116 unstructured mesh with discrete fractures, from which the full permeability tensor is
117 calculated. The aim of this workflow is to improve the representativeness of outcrops as a
118 proxy for flow in naturally fractured reservoirs, by capturing larger-scale high-resolution
119 fracture patterns covering distances comparable to well spacing in fractured reservoirs,
120 followed by modelling of aperture and flow representative of subsurface conditions. We
121 illustrate the effectiveness of the workflow using an example of 2-D fracture patterns in
122 outcropping carbonates in the Potiguar Basin, NE Brazil (Bertotti et al., accepted; de Graaf et
123 al., 2017).

2. Quantitative outcrop modelling using a UAV and photogrammetry

2.1. Image acquisition with a UAV

We use a multi-rotor UAV (Figure 2) to acquire images of multiscale fracture patterns over an area that covers several reservoir simulation grid blocks, which are subsequently merged into 2-D georeferenced outcrop models. To ensure that an area is fully covered by images with constant overlap, flight paths are programmed prior to flights (Figure 3). The programmed flights are automatically executed and controlled using a GNSS sensor (2 m accuracy) for horizontal positioning and a temperature-compensated barometer (dm-accuracy) for vertical positioning. A magnetic compass provides the absolute heading and accelerometers and a gyroscope further control the position of the UAV and ensure stable operation. Flight and environment conditions are continuously monitored and stored during flights for quality-check and diagnostic purposes.

Outcrop images are taken with a 14-megapixel compact camera in a motorised mount attached to the UAV. The resulting image resolution depends on the altitude and camera specifications. A distance of 50 m between the UAV and the surface of interest yields a resolution R of 1.44 cm/px, which changes linearly with changing distance H (in m):

$$R = \frac{100w_s H}{w_i F_r} , \quad (1.1)$$

where w_s is the camera sensor width (in mm), w_i is the image width (in pixels) and F_r is the real focal length (in mm) for the focal length in a 35 mm equivalent (F_{35}):

$$F_r = \frac{F_{35} w_s}{34.6} . \quad (1.2)$$

145 Depending on outcrop size and required resolution, most flights are between 20-100 m
146 altitude, corresponding to resolutions of 0.6-2.9 cm/px respectively. For each image, the
147 corresponding UAV position (horizontal coordinates and altitude) and orientation are
148 determined using the GNSS sensor and barometer. To further constrain the outcrop position,
149 brightly marked GCPs (Ground Control Points) are positioned on the outcrop surface, which
150 are georeferenced with a GPS, and we measure the distance between these points using a
151 hand-held laser range finder for further scaling of the model.

152 2.2. Outcrop model construction using photogrammetry

153 Using Agisoft PhotoScan®, we process the UAV images and location data into
154 georeferenced 2-D and 3-D outcrop models. This workflow consists of image alignment,
155 point cloud generation, surface meshing and texturing (Figure 4 and Figure 5).

156 2.2.1. Image alignment

157 The approximate position from where each image is taken, is used to identify the image pairs
158 that are likely to overlap. Common points are identified and extracted and positioned in 3-D
159 in a *sparse point cloud* (Figure 4a). The vertical position of a point is determined from the
160 relative change in position in the partly overlapping images, where one point is imaged from
161 different angles.

162 2.2.2. Point cloud generation

163 Once images are aligned, all points from the aligned images are extracted and positioned in 3-
164 D to generate a *dense point cloud* (Figure 4b and Figure 5a). Depending on flight altitude, the
165 point cloud can have a resolution that is similar to LiDAR datasets. A single flight at 50 m
166 altitude, capturing 100 images covering an area of 200 m × 200 m, results in a dense point
167 cloud of 1.4×10^7 points (35 points per m^2 ; Figure 4b). Higher-detail models, for example

168 captured from an altitude of 3m, yield point clouds of 8.6×10^7 points for an area of $20 \text{ m} \times 30$
169 m (1.4×10^4 points per m^2 ; Figure 5a).

170 When the images are georeferenced, aligning and dense point cloud generation are
171 relatively fast processes that can be completed during a fieldwork campaign, providing an
172 almost immediate data check to analyse whether data acquisition was successful or additional
173 flights are required. Furthermore, having already a high-resolution point cloud in the field can
174 be useful in identifying interesting features or sections of the outcrop that warrant further
175 inspection, or additional higher-resolution flights.

176 2.2.3. *Surface generation*

177 Interpretation of outcropping features requires converting the point cloud into a meshed
178 surface consisting of triangulated elements (Figure 5). The meshed surface can have the same
179 resolution as the dense point cloud, but for sub-horizontal pavements a downsampled mesh is
180 typically sufficient. For this example, the point cloud consists of 8.6×10^7 points whereas the
181 resulting surface is downsampled to 2×10^6 elements (Figure 5b,c). This surface has a
182 sufficiently high resolution for 2-D fracture interpretation. After surface generation, the
183 outcrop model can be exported as a 3-D textured geometry to geological modelling software
184 or as 2-D georeferenced orthomosaic images to GIS-based software.

185 2.3. *Fracture digitisation*

186 Fractures in the 2-D orthomosaic images are digitised in GIS-tools such as DigiFract
187 (Hardebol and Bertotti, 2013). Fracture lengths are manually traced, and attributes including
188 orientation and infill can be assigned. Manual interpretation is time-intensive, but automatic
189 tracking methods are not sufficiently sophisticated to replace manual interpretation, and
190 require time-intensive quality-checking and manual corrections (Duelis Viana et al., 2016;
191 Lin et al., 2015; Vasuki et al., 2014).

192 After digitisation, orientation, spacing and length distributions are calculated (Figure
193 6). Length or height is plotted using frequency distributions (Figure 6c,d). The orientation
194 distribution is visualised using rose diagrams or stereoplots (Figure 6b). Fracture spacing is
195 calculated using a combination of methods, where P_{10} intensity, which is the 1-D fracture
196 density measured along a line (Dershowitz, 1985), is calculated using a large amount of
197 closely-spaced scanlines, which are projected along the entire height or length of an outcrop
198 (Hardebol and Bertotti, 2013). Alternatively, spacing is defined by P_{21} intensity, which is the
199 total fracture length versus outcrop area (Dershowitz, 1985), calculated by summing the total
200 length or height of fractures within the entire outcrop or in individual beds as a function of
201 outcrop area (Wu and Pollard, 2002). The P_{21} method is sensitive to boundary effects, as the
202 length of fractures that intersect the boundary cannot be fully quantified, resulting in a
203 potential underestimation of length (Mauldon, 1998; Pahl, 1981; Zhang and Einstein, 1998).
204 Using circular sampling windows and correction methods, this can be compensated for
205 (Mauldon et al., 2001), but alternatively fractures that intersect the sampling boundary can be
206 identified and excluded from the length analysis entirely.

207 The full spacing distribution is analysed using box-counting methods (Bonnet et al.,
208 2001), where the outcrop is either divided into boxes with a constant area, in which P_{21}
209 intensity is calculated (Figure 6e), or the P_{21} intensity is calculated within a circle with a fixed
210 centre and an increasing radius (Bonnet et al., 2001; Reith, 2015). The latter method also
211 provides a means for characterising the Representative Elementary Area (REA), which is an
212 indication for the optimal grid cell size for upscaled fracture flow modelling (Dershowitz and
213 Doe, 1997; Long and Witherspoon, 1985). These methods help to identify whether the
214 digitised networks follow power-law scaling trends (Bonnet et al., 2001; Bour and Davy,
215 1997; Davy et al., 1990).

216 The size and spacing distributions are corrected for censoring artefacts, which result
217 from fractures that are not fully captured in the model such that their true length or height is
218 unknown (Bonnet et al., 2001; Ortega et al., 2006). We correct for this by filtering all
219 fractures that intersect the user-defined outcrop boundaries and by manually identifying and
220 excluding areas obscured by for example trees. Truncation artefacts, which are related to the
221 resolution limit of the outcrop model such that the smallest fractures are typically under-
222 represented, cannot be corrected automatically. Truncated length and spacing scales need to
223 be identified by the user, based on the image resolution limit.

224 **3. Finite Element meshing and stress modelling**

225 The 2-D fracture networks are meshed for mechanical and flow modelling, using
226 unstructured FE meshes with explicit fractures. The meshing and the subsequent
227 geomechanical simulations are done using ABAQUS CAE® (Dassault Systèmes®).
228 Compared to other meshing tools, we find that this tool can handle meshing of more complex
229 geometries, with minimal pre- and postprocessing.

230 *3.1. Meshing of discrete fractures*

231 Accurate representation of fracture connectivity and topology is essential, particularly when
232 the matrix is close to impermeable (Figure 7) (Hardebol et al., 2015; Sanderson and Nixon,
233 2015). **To ensure that fracture connections and intersections are correct, most GIS tools have**
234 **manual or automatic snapping options that can be used. The topology** is converted to a CAD
235 file that forms the basis for the FE model. To avoid boundary effects, rectangular model
236 boundaries are used with an intact rock buffer zone between the fracture network and model
237 boundary (Figure 8). The model is meshed using quadratic plane strain elements, with
238 refinements along the fractures (Figure 9). To avoid singularity issues, we further refine the
239 mesh around fracture tips. To model fracture opening and closing, fractures are represented

240 as seams in the mesh, using a set of post-processing functions written in Python that update
 241 the mesh to generate seams (Figure 10). A seam is generated by duplicating nodes along a
 242 seam and splitting the mesh (Figure 11). The individual seams are generated sequentially,
 243 taking into account existing seams. Except for the intersecting seams, the output mesh is
 244 identical to the input mesh, and can be read directly into the FE simulator for analysis of the
 245 stress distribution in a complex fracture network.

246 3.2. Geomechanical FE model set-up

247 Using the ABAQUS Implicit solver, the local stress state is modelled, from which fracture
 248 apertures can be derived using stress-aperture relations (Bisdom et al., 2016b). These models
 249 take into account a far-field differential stress applied to the boundaries as pressure loads
 250 (Figure 8). Maximum and minimum principle stresses are applied perpendicular to the model
 251 boundaries in a stress initialisation step, during which movement of fracture planes and
 252 boundaries is constrained. After successful stress initialisation, the displacement conditions
 253 are released to let the model equilibrate (Figure 8), solving for the stress tensor σ in fully
 254 elastic rocks (Nick et al., 2011):

$$255 \quad \sigma = D_C (\varepsilon - \varepsilon_0) + \sigma_0, \quad (1.3)$$

256 where ε and ε_0 are the strain and initial strain vectors, σ_0 is the initial stress vector and D_C is
 257 the material stiffness matrix:

$$258 \quad D_C = \frac{E}{(1+\nu)(1-2\nu)} \begin{bmatrix} 1-\nu & \nu & 0 \\ \nu & 1-\nu & 0 \\ 0 & 0 & 1-2\nu \end{bmatrix}, \quad (1.4)$$

259 with Young's modulus E and Poisson's ratio ν .

260 The slip tendency of fractures can be defined by a linear Mohr-Coulomb friction
 261 coefficient or non-linear behaviour, e.g. Barton-Bandis conductive shearing (Bisdom et al.,

262 2016b), which can be defined by functions or look-up tables. A heterogeneous or constant
263 pore pressure distribution can also be taken into account, as well as single-phase flow
264 injection to take into account localised changes in pore pressure over time (Bisdom et al.,
265 2016a).

266 3.3. Aperture modelling

267 For each fracture node, stress-dependent apertures are calculated from the local normal and
268 shear stresses in the geomechanical FE model (Figure 12). Different stress-aperture relations
269 can be used to calculate the corresponding spatial aperture distribution, capturing small-scale
270 variations along individual fractures (Appendix A; Bisdom et al., 2016d). Aperture
271 definitions that are not a function of stress, such as power-law scaling, are calculated using
272 Python functions in a GIS environment, where aperture is calculated for each fracture
273 segment based on the geometrical properties of that segment. Using the x,y -positions, these
274 values are translated from the segments to the nodes of the mesh (Bisdom et al., 2016c,
275 2016d). Four commonly-used aperture definitions have been implemented into the workflow,
276 but other definitions can be easily added. These definitions are (sub-)linear length aperture
277 scaling predicted by LEFM, power-law scaling and Barton-Bandis conductive shearing
278 derived from either FE models or geometrical approximations (Appendix A).

279 4. Flow modelling

280 To construct the flow model, we use the workflow from (Bisdom et al., 2016b) summarised
281 below. Here, we extend this workflow from calculating only equivalent permeability parallel
282 to the edges of the model to calculating the full permeability tensor to derive the principal
283 maximum and minimum permeability values.

284 Flow is modelled using the same FE mesh used for the geomechanical models, where
285 the seams in the mesh have been replaced by lower-dimensional elements to which modelled

286 fracture apertures are assigned (Bisdorn et al., 2016b). In addition, the buffer zone added to
 287 avoid stress boundary effects is removed such that fractures intersect the edges of the model.
 288 We use a hybrid Finite-Element Finite-Volume (FE-FV) approach implemented in the
 289 Complex Systems Modelling Platform to solve the flow equations (Matthäi et al., 2007).

290 **Similar to Durlofsky (1991)**, the full equivalent permeability tensor (\mathbf{k}) is computed
 291 by solving the steady state continuity equation for flow in different directions using a far-field
 292 pressure gradient applied in both horizontal directions of the rectangular 2-D pavements.
 293 Note that the superscripts 1 and 2 are used for these two problems in Eq. (1.5) and a constant
 294 viscosity (μ) is assumed. This is followed by volume-averaging (for both problems $\langle \cdot \rangle^1, \langle \cdot \rangle^2$)
 295 of resulted fluid velocities (u_x and u_y) and pressure gradients ($\nabla p_x, \nabla p_y$) to solve for
 296 equivalent tensor permeability through:

$$297 \quad \langle \nabla p \rangle \mathbf{k} = -\mu \langle u \rangle \Rightarrow \begin{bmatrix} \langle \nabla p_x \rangle^1 & \langle \nabla p_y \rangle^1 & 0 & 0 \\ 0 & 0 & \langle \nabla p_x \rangle^1 & \langle \nabla p_y \rangle^1 \\ \langle \nabla p_x \rangle^2 & \langle \nabla p_y \rangle^2 & 0 & 0 \\ 0 & 0 & \langle \nabla p_x \rangle^2 & \langle \nabla p_y \rangle^2 \\ 0 & 1 & -1 & 0 \end{bmatrix} \begin{Bmatrix} k_{xx} \\ k_{xy} \\ k_{yx} \\ k_{yy} \end{Bmatrix} = -\mu \begin{Bmatrix} \langle u_x \rangle^1 \\ \langle u_y \rangle^1 \\ \langle u_x \rangle^2 \\ \langle u_y \rangle^2 \\ 0 \end{Bmatrix}. \quad (1.5)$$

298 The maximum and minimum principal permeability values (k_{\max}, k_{\min}) as well as the
 299 principal direction (θ) can be calculated.

300 **5. Application**

301 The integrated workflow is applied to model permeability through an outcropping network of
 302 fractures in the Jandaíra Formation, which is a carbonate formation that crops out in large
 303 parts of the Potiguar Basin in NE Brazil. **Extensive fracture networks were formed**
 304 **predominantly during burial in a compressional setting (Bertotti et al., **accepted**; de Graaf et**

305 al., 2017). The sub-horizontal position of the rocks provides excellent exposures of multiscale
306 fracture patterns covering areas of several hundred by several hundred meters, which is
307 comparable to the spacing of wells in a fractured reservoir (Bisdorn et al., **accepted**). In
308 conventional reservoir models, these areas are typically populated with stochastic fractures
309 whose distributions are derived from well data or small outcrops. We use our workflow to
310 capture and create a deterministic discrete fracture flow model, focusing on a rectangular area
311 of a pavement in the western part of the basin in which there is a minimal impact of censoring
312 caused by a few trees (Figure 13). This study area is ideal for 2-D geomechanical and flow
313 analysis, as all fractures dip perpendicular to the sub-horizontal bedding planes (Bisdorn et
314 al., **accepted**). Hence, spacings and lengths interpreted on the pavements do not require any
315 Terzaghi corrections, and the complete orientation distribution can be quantified by digitising
316 fracture strikes. Geometrical analysis of fractures in the Potiguar basin is outside the scope of
317 this work, but presented elsewhere (Bertotti et al., **accepted**; Bisdorn et al., **accepted**; de
318 Graaf et al., 2017).

319 5.1. Fracture network geometry

320 The area of interest was imaged with the UAV at an altitude of 50 m above the ground,
321 resulting in 90 images with a resolution of 1.44 cm/px. The model was accurately
322 georeferenced using several GCPs, for which we measured the absolute position and the
323 distance between the GCPs. The resulting dense point cloud covers an area of $4.1 \times 10^4 \text{ m}^2$
324 with a point density of 284 m^{-1} . The georeferenced orthomosaic has the same resolution as
325 the individual images (1.44 cm/px; Figure 13). Using DigiFract, we digitised 1082 fractures
326 in a rectangular area of $150 \text{ m} \times 142 \text{ m}$ (Figure 14b). Three orientation families were
327 identified with size and spacing distributions that follow power-law scaling trends (Bisdorn et
328 al., **accepted**). Weathering has affected apertures and limits the view of the smallest fracture
329 scales (i.e. smaller than 1 m), but these smaller length scales have only a relatively small

330 impact on permeability compared to the large connected system of fractures. Recent
331 weathering also created dendritic dissolution patterns, which are excluded from the analysis.

332 5.2. *Fracture aperture distribution*

333 Most fractures are open and free from cement, i.e. barren, but this is associated with
334 exhumation and weathering (Bertotti et al., **accepted**). To define apertures representative of
335 subsurface conditions, we use a sublinear length-aperture scaling model defined by Linear
336 Elastic Fracture Mechanics (LEFM; Atkinson, 1984; Bisdorf et al., 2016c; Lawn and
337 Wilshaw, 1975; Olson, 2003). The far-field stress is defined by a 30 MPa σ_1 applied as
338 pressure loads perpendicular to the north and south boundaries and a σ_3 of 10 MPa oriented
339 E-W. These stress directions are comparable to the paleostress directions under which most
340 of the fractures were formed (Bertotti et al., **accepted**). In the absence of measurements of the
341 elastic rock properties, the rock is assumed fully elastic with a Poisson's ratio of 0.3 and a
342 Young's modulus of 50 GPa. The model mesh consists of 5.1×10^5 triangulated elements
343 (Figure 14a).

344 The resulting aperture scales with length and stress (Figure 14b). Aperture follows a
345 lognormal distribution with a maximum of 2.5 mm and an average of 0.5 mm. One percent of
346 fractures is hydraulically closed, but the majority of the network is permeable (Figure 14c,d).

347 5.3. *Equivalent permeability*

348 For a 1 mD matrix, the pressure gradient in the x - and y -directions is highly heterogeneous,
349 particularly in the x -direction (Figure 14c,d). We quantify permeability as the ratio between
350 equivalent and matrix permeability, which quantifies the contrast between matrix and
351 fractures (Figure 15). The ratio is high for a low matrix permeability, as most flow is carried
352 by the fractures, and decreases for increasing matrix permeability. For a low permeability

353 matrix (1 mD), fracture flow in the y -direction is more dominant than the x -direction (Figure
354 15a,b), but remarkably this is reversed for higher matrix permeabilities (Figure 15c,d).

355 This reversal is better quantified using the fluid velocities, which show that one large
356 fracture percolates through the entire model in the y -direction, creating a flow pathway even
357 when matrix permeability is low (Figure 15a,b). There are several large E-W striking
358 fractures with large apertures, but they do not fully percolate the model, limiting their impact
359 in a low-permeability matrix.

360 This change in permeability is better explained by calculating the full permeability
361 tensor (Figure 16). For matrix permeabilities below 100 mD, maximum permeability is in a
362 NE-SW direction. In this domain, permeability is controlled by fracture flow. For increasing
363 matrix permeability, flow is carried by a mix of fractures and matrix, and the maximum
364 permeability rotates to ENE-WSW, remaining anisotropic. Only when matrix permeability is
365 larger than several Darcy, flow is fully carried by the matrix and permeability becomes
366 isotropic. However, for most models, the highly-connected high-intensity fracture network
367 controls flow either completely or partly.

368 **6. Discussion**

369 *6.1. From outcrops to representative subsurface flow models*

370 Contrary to other studies, the presented workflow uses only the outcropping network
371 geometry as input for deterministic flow models, not taking into account outcropping
372 apertures. Instead, we use geomechanical FE models to solve the stress state around the
373 fracture network, based on estimates of subsurface stress conditions and rock properties.
374 These geomechanical parameters can typically be derived from subsurface datasets, albeit
375 with uncertainty ranges. However, the applied methodology is fast, allowing the inclusion of
376 uncertainty ranges. The resulting stress states are used to calculate aperture, using different

377 stress-aperture relations (Bisdom et al., 2016d). This combination of outcropping geometries
378 and subsurface stress states and aperture distributions results in models that are more
379 representative of fractured reservoir permeability compared to analogue studies that use
380 apertures of exhumed barren fractures or assume a constant aperture for the entire network
381 (Makedonska et al., 2016).

382 **Laser scanning of outcrops is an alternative method that provides deterministic**
383 **representations of entire outcrops, but photogrammetry offers more flexibility (Hodgetts,**
384 **2013).** Through the use of deterministic 2-D patterns rather than stochastic fracture networks
385 derived from 1-D distributions, more realistic estimates of permeability can be made.
386 Stochastic models typically contain mutually crosscutting networks of fractures resulting in
387 highly connected networks with consistently high permeabilities, which does not correspond
388 to observations of permeability heterogeneity typically observed in fractured reservoirs. The
389 studied deterministic pattern better represents natural fracture topology with terminating
390 rather than fully crosscutting fractures (Hardebol et al., 2015; Sanderson and Nixon, 2015).

391 *6.2. Lessons for reservoir-scale flow modelling*

392 The studied fracture network from the Potiguar basin contains predominantly N-S and E-W
393 striking fractures that form an orthogonal pattern. Orthogonal patterns are observed in many
394 fractured outcrops and are assumed to be present in many subsurface reservoirs (Bai et al.,
395 2002). In reservoir-scale flow models, these patterns are upscaled to effective properties in
396 the two dominant fracture directions that are assumed to be representative of fracture
397 permeability, comparable to the equivalent permeability in the x - and y -directions. However,
398 by only considering flow in two directions, permeability is underestimated in this example, as
399 for a 1 mD matrix permeability, the permeability ratio in x - and y -directions is 1.9×10^3 and
400 2.2×10^3 respectively, whereas the maximum ratio is 3.9×10^3 in the NE-SW direction. Even
401 for these relatively homogeneous orthogonal networks, the absolute maximum permeability

402 cannot be accurately determined using conventional upscaling. The outcrop-derived 2-D
403 permeability tensor models can be used to determine the principal permeabilities of discrete
404 fracture networks covering several grid cells, as a more accurate alternative to quantify
405 permeability compared to ODA upscaling (Oda, 1985). These flow models also help to
406 identify different fracture-matrix permeability domains, which can be used to better
407 characterise fractured reservoir flow domains. To further bridge the gap between discrete
408 fracture models and reservoir-scale continuum models, hybrid upscaling techniques can be
409 used (Egya et al., 2016; Shah et al., 2016).

410 **7. Conclusions**

411 Outcrops provide a wealth of data for studying and modelling of fracture networks, which
412 cannot be fully captured with 1-D scanlines, as these only capture spacing and aperture of one
413 orientation set. LiDAR on the other hand captures entire **outcrops at a high resolution**, but
414 this method has limited flexibility in terms of the type of outcrops it can be applied to and in
415 terms of processing (Hodgetts, 2013). **The presented workflow enables fast generation of**
416 **highly detailed realistic fracture networks for use of geomechanical and flow modelling,**
417 **variations of which have been applied to study different aspects of fracture and fracture-**
418 **matrix flow (e.g. Aljuboori et al., 2015; Arnold et al., 2016; Bisdorn et al., 2016c; Egya et al.,**
419 **2016; Muhammad, 2016; Shah et al., 2016).**

420 We use fracture patterns derived from these models for geomechanical and flow
421 modelling of discrete fractures on a scale that is representative of part of a fractured reservoir,
422 spanning an area of several conventional reservoir grid cells. The geomechanical model
423 solves the local stress state within the fracture network, which is used to model aperture using
424 a range of stress-aperture relations. The flow models consider matrix and fracture flow.
425 Although the fluid pressure in the x - and y -directions of these models can be used to quantify

426 relative permeability differences between different models, it is not representative of the true
427 principal permeabilities, even in an orthogonal network where fractures strike mainly parallel
428 to the x - and y -directions. The presented workflow allows for fast quantification of the full
429 permeability tensor in domains covering several conventional simulator grid cells using
430 realistic fracture patterns digitised from outcrops, with minimal pre-processing and no
431 upscaling.

432 **Acknowledgements**

433 Total S.A. is thanked for sponsoring the PhD of the first author. The fracture patterns from
434 the Potiguar basin were acquired with financial support from the National Petroleum Agency
435 (ANP) of Brazil and Petrobras and with support in the field from numerous students from the
436 VU University and Delft University of Technology in the Netherlands and F.H. Bezerra and
437 his students from the Federal University of Rio Grande Do Norte (UFRN) in Brazil. The
438 fracture data from Tunisia has been acquired with support from S. Bouaziz and A. Hammami
439 from ENIS in Sfax, Tunisia. We thank N.J. Hardebol from Delft University of Technology
440 and W. van der Zee and M. Holland from Baker Hughes for fruitful discussions and support
441 regarding the geomechanical modelling, and S. Geiger for his input regarding flow
442 modelling. We thank editor Gregoire Mariethoz, Andrea Billi and four anonymous reviewers
443 for their suggestions to improve the earlier version of this manuscript.

444 **References**

- 445 Aljuboori, F., Corbett, P., Bisdorn, K., Bertotti, G., Geiger, S., 2015. Using Outcrop Data for
446 Geological Well Test Modelling in Fractured Reservoirs, in: 77th EAGE Conference
447 and Exhibition 2015. doi:10.3997/2214-4609.201413037
- 448 Arnold, D., Demyanov, V., Christie, M., Bakay, A., Gopa, K., 2016. Optimisation of decision

449 making under uncertainty throughout field lifetime: A fractured reservoir example.
450 Comput. Geosci. 95, 123–139. doi:10.1016/j.cageo.2016.07.011

451 Atkinson, B.K., 1984. Subcritical crack growth in geological materials. J. Geophys. Res. 89,
452 4077. doi:10.1029/JB089iB06p04077

453 Baghbanan, A., Jing, L., 2008. Stress effects on permeability in a fractured rock mass with
454 correlated fracture length and aperture. Int. J. Rock Mech. Min. Sci. 45, 1320–1334.
455 doi:10.1016/j.ijrmms.2008.01.015

456 Bai, T., Maerten, L., Gross, M.R., Aydin, A., 2002. Orthogonal cross joints: do they imply a
457 regional stress rotation? J. Struct. Geol. 24, 77–88. doi:10.1016/S0191-8141(01)00050-5

458 Bandis, S., 1980. Experimental Studies of Scale Effects on Shear Strength and Deformation
459 of Rock Joints. University of Leeds. doi:10.12681/eadd/4686

460 Bandis, S.C., Lumsden, a. C., Barton, N.R., 1983. Fundamentals of rock joint deformation.
461 Int. J. Rock Mech. Min. Sci. Geomech. Abstr. 20, 249–268. doi:10.1016/0148-
462 9062(83)90595-8

463 Barton, N., 2014. Non-linear behaviour for naturally fractured carbonates and frac-stimulated
464 gas-shales. First Break 32, 51–66. doi:10.3997/1365-2397.2014011

465 Barton, N., 1982. Modelling rock joint behaviour from in situ block tests: Implications for
466 nuclear waste repository design. Columbus, OH.

467 Barton, N., Bandis, S., 1980. Some effects of scale on the shear strength of joints, in:
468 International Journal of Rock Mechanics and Mining Sciences & Geomechanics
469 Abstracts. Pergamon Press Ltd., pp. 69–73. doi:http://dx.doi.org/10.1016/0148-
470 9062(80)90009-1

471 Barton, N., Bandis, S., Bakhtar, K., 1985. Strength, deformation and conductivity coupling of

472 rock joints. *Int. J. Rock Mech. Min. Sci. Geomech. Abstr.* 22, 121–140.
473 doi:10.1016/0148-9062(85)93227-9

474 Barton, N., Choubey, V., 1977. The shear strength of rock joints in theory and practice. *Rock*
475 *Mech. Felsmechanik Mec. des Roches* 10, 1–54. doi:10.1007/BF01261801

476 Belayneh, M.W., Matthäi, S.K., Blunt, M.J., Rogers, S.F., 2009. Comparison of deterministic
477 with stochastic fracture models in water-flooding numerical simulations. *Am. Assoc.*
478 *Pet. Geol. Bull.* 93, 1633–1648. doi:10.1306/07220909031

479 Bemis, S.P., Micklethwaite, S., Turner, D., James, M.R., Akciz, S., Thiele, S.T., Bangash,
480 H.A., 2014. Ground-based and UAV-Based photogrammetry: A multi-scale, high-
481 resolution mapping tool for structural geology and paleoseismology. *J. Struct. Geol.* 69,
482 163–178. doi:10.1016/j.jsg.2014.10.007

483 Bertotti, G., de Graaf, S., Bisdom, K., Vonhof, H.B., Reijmer, J.J.G., Bezerra, F.H.R.,
484 Cazarin, C., **accepted**. Fracturing and flow during post-rift subsidence in carbonate
485 rocks of the Jandaira Formation (NE Brazil). *Basin Res.*

486 Bisdom, K., Baud, E., Estrada, S., Sanz-Perl, Y., Gauthier, B., Bertotti, G., 2016a. Coupled
487 Stress-fluid Pressure Modelling of Stimulated Rock Volume in Shale - Impact of Natural
488 Fractures and Beef, in: 78th EAGE Conference & Exhibition. EAGE, Vienna, Austria.

489 Bisdom, K., Bertotti, G., Bezerra, F.H., **accepted**. Inter-well scale natural fracture geometry
490 and permeability variations in low-deformation carbonate rocks. *J. Struct. Geol.*

491 Bisdom, K., Bertotti, G., Nick, H.M., 2016b. The impact of in-situ stress and outcrop-based
492 fracture geometry on hydraulic aperture and upscaled permeability in fractured
493 reservoirs. *Tectonophysics* 690, 63–75. doi:10.1016/j.tecto.2016.04.006

494 Bisdom, K., Bertotti, G., Nick, H.M., 2016c. A geometrically based method for predicting

495 stress-induced fracture aperture and flow in discrete fracture networks. *Am. Assoc. Pet.*
496 *Geol. Bull.* 100, 1075–1097. doi:10.1306/02111615127

497 Bisdom, K., Bertotti, G., Nick, H.M., 2016d. The impact of different aperture distribution
498 models and critical stress criteria on equivalent permeability in fractured rocks. *J.*
499 *Geophys. Res. Solid Earth* 121, 4045–4063. doi:10.1002/2015JB012657

500 Bisdom, K., Gauthier, B.D.M., Bertotti, G., Hardebol, N.J., 2014. Calibrating discrete
501 fracture-network models with a carbonate three-dimensional outcrop fracture network:
502 Implications for naturally fractured reservoir modeling. *Am. Assoc. Pet. Geol. Bull.* 98,
503 1351–1376. doi:10.1306/02031413060

504 Bond, C.E., Shackleton, J.R., Wild, T., 2015. From Field Fractures to Reservoir Prediction:
505 Utilizing Drones, Virtual Outcrop and Digital Data Analysis to Input Into Discrete
506 Fracture Network (DFN) Models, in: AAPG Annual Convention and Exhibition.
507 Denver, Colorado.

508 Bonnet, E., Bour, O., Odling, N.E., Davy, P., Main, I., Cowie, P., Berkowitz, B., 2001.
509 Scaling of fracture systems in geological media. *Rev. Geophys.* 39, 347–383.
510 doi:10.1029/1999RG000074

511 Bour, O., Davy, P., 1997. Connectivity of random fault networks following a power law fault
512 length distribution. *Water Resour. Res.* 33, 1567–1583. doi:10.1029/96WR00433

513 Cottureau, N., Garcia, M.H., Gosselin, O.R., Vigier, L., 2010. Effective Fracture Network
514 Permeability: Comparative Study of Calculation Methods, in: SPE EUROPEC/EAGE
515 Annual Conference and Exhibition. Society of Petroleum Engineers, Barcelona, Spain.
516 doi:10.2118/131126-ms

517 Davy, P., Sornette, A., Sornette, D., 1990. Some consequences of a proposed fractal nature of

518 continental faulting. *Nature* 348, 56–58. doi:10.1038/348056a0

519 de Graaf, S., Reijmer, J.J.G., Bertotti, G. V., Bezerra, F.H.R., Cazarin, C.L., Bisdorn, K.,
520 Vonhof, H.B., 2017. Fracturing and calcite cementation controlling fluid flow in the
521 shallow-water carbonates of the Jandaíra Formation, Brazil. *Mar. Pet. Geol.* 80, 382–
522 393. doi:10.1016/j.marpetgeo.2016.12.014

523 Dershowitz, W., 1985. Rock joint systems (Ph.D. Thesis). MIT. Massachusetts Institute of
524 Technology.

525 Dershowitz, W., Doe, T., 1997. Analysis of heterogeneously connected rock masses by
526 forward modeling of fractional dimension flow behavior. *Int. J. Rock Mech. Min. Sci.*
527 34, 61.e1-61.e19. doi:10.1016/S1365-1609(97)00237-2

528 Duelis Viana, C., Endlein, A., Ademar da Cruz Campanha, G., Henrique Grohmann, C.,
529 2016. Algorithms for extraction of structural attitudes from 3D outcrop models. *Comput.*
530 *Geosci.* 90, 112–122. doi:10.1016/j.cageo.2016.02.017

531 Durlafsky, L.J., 1991. Numerical calculation of equivalent grid block permeability tensors for
532 heterogeneous porous media. *Water Resour. Res.* 27, 699–708.
533 doi:10.1029/91WR00107

534 Egya, D., Geiger, S., Corbett, P., Bisdorn, K., Bertotti, G., Bezerra, H., 2016. Assessing the
535 Validity and Limitations of Dual- porosity Models Using Geological Well Testing for
536 Fractured Formations, in: 78th EAGE Conference & Exhibition. EAGE, Vienna,
537 Austria.

538 Fabuel-Perez, I., Hodgetts, D., Redfern, J., 2010. Integration of digital outcrop models
539 (DOMs) and high resolution sedimentology – workflow and implications for geological
540 modelling: Oukaimeden Sandstone Formation, High Atlas (Morocco). *Pet. Geosci.* 16,

541 133–154. doi:10.1144/1354-079309-820

542 Geiger, S., Hehmeyer, O., Agada, S., Mutti, M., Benson, G., Shekhar, R., Toigulova, G.,
543 Chen, F., Christ, N., Amour, F., Agar, S., Immenhauser, A., 2013. Deciphering the
544 Fundamental Controls of Flow in Carbonates Using Numerical Well-Testing, Production
545 Optimisation, and 3D High-resolution Outcrop Analogues for Fractured Carbonate
546 Reservoirs, in: Proceedings of 75th EAGE Conference & Exhibition Incorporating SPE
547 EUROPEC 2013. Society of Petroleum Engineers. doi:10.2118/164805-MS

548 Geiger, S., Matthäi, S., 2012. What can we learn from high-resolution numerical simulations
549 of single- and multi-phase fluid flow in fractured outcrop analogues? Geol. Soc.
550 London, Spec. Publ. 374, 125–144. doi:10.1144/SP374.8

551 Hardebol, N.J., Bertotti, G., 2013. DigiFract: A software and data model implementation for
552 flexible acquisition and processing of fracture data from outcrops. Comput. Geosci. 54,
553 326–336. doi:10.1016/j.cageo.2012.10.021

554 Hardebol, N.J., Maier, C., Nick, H., Geiger, S., Bertotti, G., Boro, H., 2015. Multiscale
555 fracture network characterization and impact on flow: A case study on the Latemar
556 carbonate platform. J. Geophys. Res. Solid Earth 120, 8197–8222.
557 doi:10.1002/2015JB011879

558 Harwin, S., Lucieer, A., 2012. Assessing the accuracy of georeferenced point clouds
559 produced via multi-view stereopsis from Unmanned Aerial Vehicle (UAV) imagery.
560 Remote Sens. 4, 1573–1599. doi:10.3390/rs4061573

561 Hodgetts, D., 2013. Laser scanning and digital outcrop geology in the petroleum industry: A
562 review. Mar. Pet. Geol. 46, 335–354. doi:10.1016/j.marpetgeo.2013.02.014

563 Hooker, J.N., Gale, J.F.W., Gomez, L.A., Laubach, S.E., Marrett, R., Reed, R.M., 2009.

564 Aperture-size scaling variations in a low-strain opening-mode fracture set, Cozzette
565 Sandstone, Colorado. *J. Struct. Geol.* 31, 707–718. doi:10.1016/j.jsg.2009.04.001

566 Hooker, J.N., Laubach, S.E., Marrett, R., 2014. A universal power-law scaling exponent for
567 fracture apertures in sandstones. *Geol. Soc. Am. Bull.* 126, 1340–1362.
568 doi:10.1130/B30945.1

569 James, M.R., Robson, S., 2012. Straightforward reconstruction of 3D surfaces and
570 topography with a camera: Accuracy and geoscience application. *J. Geophys. Res. Earth
571 Surf.* 117, 1–17. doi:10.1029/2011JF002289

572 Jonoud, S., Jackson, M.D., 2008. Validity of Steady-State Upscaling Techniques. *SPE
573 Reserv. Eval. Eng.* 11, 405–416. doi:10.2118/100293-PA

574 Karimi-Fard, M., Durlofsky, L.J., 2016. A general gridding, discretization, and coarsening
575 methodology for modeling flow in porous formations with discrete geological features.
576 *Adv. Water Resour.* m, 354–372. doi:10.1016/j.advwatres.2016.07.019

577 Lang, P.S., Paluszny, A., Zimmerman, R.W., 2014. Permeability tensor of three-dimensional
578 fractured porous rock and a comparison to trace map predictions. *J. Geophys. Res. Solid
579 Earth* 119, 6288–6307. doi:10.1002/2014JB011027

580 Lawn, B.R., Wilshaw, T.R., 1975. *Fracture of brittle solids*. Cambridge University Press.

581 Lei, Q., Latham, J., Xiang, J., Tsang, C.-F., 2015. Polyaxial stress-induced variable aperture
582 model for persistent 3D fracture networks. *Geomech. Energy Environ.* 1, 34–47.
583 doi:10.1016/j.gete.2015.03.003

584 Lei, Q., Latham, J.-P., Xiang, J., Tsang, C.-F., Lang, P., Guo, L., 2014. Effects of
585 geomechanical changes on the validity of a discrete fracture network representation of a
586 realistic two-dimensional fractured rock. *Int. J. Rock Mech. Min. Sci.* 70, 507–523.

587 doi:10.1016/j.ijrmms.2014.06.001

588 Lei, Q., Wang, X., Xiang, J., Latham, J.-P., 2016. Influence of stress on the permeability of a
589 three-dimensional fractured sedimentary layer. 50th US Rock Mech. / Geomech. Symp.
590 586.

591 Lin, Y., Jiang, M., Yao, Y., Zhang, L., Lin, J., 2015. Use of UAV oblique imaging for
592 detection of individual trees in residential environments. Urban For. Urban Green. 14,
593 404–412. doi:10.1016/j.ufug.2015.03.003

594 Long, J.C.S., Witherspoon, P.A., 1985. The relationship of the degree of interconnection to
595 permeability in fracture networks. J. Geophys. Res. 90, 3087.
596 doi:10.1029/JB090iB04p03087

597 Mahmud, K., Mariethoz, G., Treble, P.C., Baker, A., 2015. Terrestrial LiDAR Survey and
598 Morphological Analysis to Identify Infiltration Properties in the Tamala Limestone,
599 Western Australia. IEEE J. Sel. Top. Appl. Earth Obs. Remote Sens. 8, 4871–4881.
600 doi:10.1109/JSTARS.2015.2451088

601 Makedonska, N., Hyman, J.D., Karra, S., Painter, S.L., Gable, C.W., Viswanathan, H.S.,
602 2016. Evaluating the effect of internal aperture variability on transport in kilometer scale
603 discrete fracture networks. Adv. Water Resour. 94, 486–497.
604 doi:10.1016/j.advwatres.2016.06.010

605 **Martinez-Landa, L., Carrera, J., Pérez-Estaún, A., Gomez, P., Bajos, C., 2016. Structural**
606 **geology and geophysics as a support to build a hydrogeologic model of granite rock.**
607 **Solid Earth 7, 881–895. doi:10.5194/se-7-881-2016**

608 Matthäi, S.K., Belayneh, M., 2004. Fluid flow partitioning between fractures and a permeable
609 rock matrix. Geophys. Res. Lett. 31. doi:10.1029/2003GL019027

610 Matthäi, S.K., Geiger, S., Roberts, S.G., Paluszny, A., Belayneh, M., Burri, A., Mezentsev,
611 A., Lu, H., Coumou, D., Driesner, T., Heinrich, C.A., 2007. Numerical simulation of
612 multi-phase fluid flow in structurally complex reservoirs. *Geol. Soc. London, Spec.*
613 *Publ.* 292, 405–429. doi:10.1144/SP292.22

614 **Mauldon, M., 1998. Estimating Mean Fracture Trace Length and Density from Observations**
615 **in Convex Windows. *Rock Mech. Rock Eng.* 31, 201–216. doi:10.1007/s006030050021**

616 **Mauldon, M., Dunne, W.M., Rohrbaugh, M.B., 2001. Circular scanlines and circular**
617 **windows: New tools for characterizing the geometry of fracture traces. *J. Struct. Geol.***
618 **23, 247–258. doi:10.1016/S0191-8141(00)00094-8**

619 Muhammad, F., 2016. Geological well testing in fractured carbonate reservoir. Heriot Watt
620 University.

621 Nejati, M., Paluszny, A., Zimmerman, R.W., 2016. A finite element framework for modeling
622 internal frictional contact in three-dimensional fractured media using unstructured
623 tetrahedral meshes. *Comput. Methods Appl. Mech. Eng.* 306, 123–150.
624 doi:10.1016/j.cma.2016.03.028

625 Nelson, R.A., 2001. Geologic Analysis of Naturally Fractured Reservoirs, in: *Geologic*
626 *Analysis of Naturally Fractured Reservoirs*. Gulf Professional Publishing, Woburn, MA,
627 USA, pp. 101–124.

628 Nick, H.M., Matthäi, S.K., 2011a. A Hybrid Finite-Element Finite-Volume Method with
629 Embedded Discontinuities for Solute Transport in Heterogeneous Media. *Vadose Zo. J.*
630 10, 299. doi:10.2136/vzj2010.0015

631 Nick, H.M., Matthäi, S.K., 2011b. Comparison of Three FE-FV Numerical Schemes for
632 Single- and Two-Phase Flow Simulation of Fractured Porous Media. *Transp. Porous*

633 Media 90, 421–444. doi:10.1007/s11242-011-9793-y

634 Nick, H.M., Paluszny, A., Blunt, M.J., Matthai, S.K., 2011. Role of geomechanically grown
635 fractures on dispersive transport in heterogeneous geological formations. *Phys. Rev. E*
636 84, 56301. doi:10.1103/PhysRevE.84.056301

637 Oda, M., 1985. Permeability tensor for discontinuous rock masses. *Géotechnique* 35, 483–
638 495.

639 Olson, J.E., 2003. Sublinear scaling of fracture aperture versus length: An exception or the
640 rule? *J. Geophys. Res. Solid Earth* 108, 2413. doi:10.1029/2001JB000419

641 Olson, J.E., Laubach, S.E., Lander, R.H., 2009. Natural fracture characterization in tight gas
642 sandstones: Integrating mechanics and diagenesis. *Am. Assoc. Pet. Geol. Bull.* 93,
643 1535–1549. doi:10.1306/08110909100

644 Olson, J.E., Schultz, R.A., 2011. Comment on “A note on the scaling relations for opening
645 mode fractures in rock” by C.H. Scholz. *J. Struct. Geol.* 33, 1523–1524.
646 doi:10.1016/j.jsrg.2011.07.004

647 Olsson, R., Barton, N., 2001. An improved model for hydromechanical coupling during
648 shearing of rock joints. *Int. J. Rock Mech. Min. Sci.* 38, 317–329. doi:10.1016/S1365-
649 1609(00)00079-4

650 Ortega, O.J., Marrett, R.A., Laubach, S.E., 2006. A scale-independent approach to fracture
651 intensity and average spacing measurement. *Am. Assoc. Pet. Geol. Bull.* 90, 193–208.
652 doi:10.1306/08250505059

653 Pahl, P.J., 1981. Estimating the mean length of discontinuity traces. *Int. J. Rock Mech. Min.*
654 *Sci. Geomech. Abstr.* 18, 221–228. doi:10.1016/0148-9062(81)90976-1

655 Paluszny, A., Matthäi, S.K., Hohmeyer, M., 2007. Hybrid finite element-finite volume

656 discretization of complex geologic structures and a new simulation workflow
657 demonstrated on fractured rocks. *Geofluids* 7, 186–208. doi:10.1111/j.1468-
658 8123.2007.00180.x

659 Philip, Z.G., Jennings, J.W., Olson, J.E., Laubach, S.E., Holder, J., 2005. Modeling Coupled
660 Fracture-Matrix Fluid Flow in Geomechanically Simulated Fracture Networks. *SPE*
661 *Reserv. Eval. Eng.* 8, 300–309. doi:10.2118/77340-PA

662 Pollard, D.D., Segall, P., 1987. Theoretical displacements and stresses near fractures in rock:
663 with applications to faults, veins, dikes, and solution surfaces, in: *Fracture Mechanics of*
664 *Rock*. Elsevier, pp. 277–349. doi:10.1016/B978-0-12-066266-1.50013-2

665 Reif, D., Grasemann, B., Faber, R.H., 2011. Quantitative structural analysis using remote
666 sensing data: Kurdistan, northeast Iraq. *Am. Assoc. Pet. Geol. Bull.* 95, 941–956.
667 doi:10.1306/11151010112

668 Reith, D.F.H., 2015. Analysis of the different impacts influencing the value of the fractal
669 dimension regarding the Whitby Mudstone formation (UK) & Jandaira formation
670 (Brazil). Delft University of Technology.

671 Rotevatn, A., Buckley, S.J., Howell, J.A., Fossen, H., 2009. Overlapping faults and their
672 effect on fluid flow in different reservoir types: A LIDAR-based outcrop modeling and
673 flow simulation study. *Am. Assoc. Pet. Geol. Bull.* 93, 407–427.
674 doi:10.1306/09300807092

675 Sanderson, D.J., Nixon, C.W., 2015. The use of topology in fracture network
676 characterization. *J. Struct. Geol.* 72, 55–66. doi:10.1016/j.jsg.2015.01.005

677 **Scholz, C.H., 2011. Reply to comments of Jon Olson and Richard Schultz. *J. Struct. Geol.* 33,**
678 **1525–1526. doi:10.1016/j.jsg.2011.07.006**

679 Shah, S., Møyner, O., Tene, M., Lie, K.A., Hajibeygi, H., 2016. The multiscale restriction
680 smoothed basis method for fractured porous media (F-MsRSB). *J. Comput. Phys.* 318,
681 36–57. doi:10.1016/j.jcp.2016.05.001

682 Tao, Q., Ehlig-Economides, C.A., Ghassemi, A., 2009. Investigation of Stress-Dependent
683 Permeability in Naturally Fractured Reservoirs Using a Fully Coupled Poroelastic
684 Displacement Discontinuity Model, in: *SPE Annual Technical Conference and
685 Exhibition*. Society of Petroleum Engineers, New Orleans, Louisiana.
686 doi:10.2118/124745-MS

687 Tavani, S., Corradetti, A., Billi, A., 2016. High precision analysis of an embryonic
688 extensional fault-related fold using 3D orthorectified virtual outcrops: The viewpoint
689 importance in structural geology. *J. Struct. Geol.* 86, 200–210.
690 doi:10.1016/j.jsjg.2016.03.009

691 Tavani, S., Granado, P., Corradetti, A., Girundo, M., Iannace, A., Arbués, P., Muñoz, J. a.,
692 Mazzoli, S., 2014. Building a virtual outcrop, extracting geological information from it,
693 and sharing the results in Google Earth via OpenPlot and Photoscan: An example from
694 the Khaviz Anticline (Iran). *Comput. Geosci.* 63, 44–53.
695 doi:10.1016/j.cageo.2013.10.013

696 Ullman, S., 1979. The Interpretation of Structure from Motion. *Proc. R. Soc. B Biol. Sci.* 203,
697 405–426. doi:10.1098/rspb.1979.0006

698 Vasuki, Y., Holden, E.-J., Kovesi, P., Micklethwaite, S., 2014. Semi-automatic mapping of
699 geological Structures using UAV-based photogrammetric data: An image analysis
700 approach. *Comput. Geosci.* 69, 22–32. doi:10.1016/j.cageo.2014.04.012

701 Vermilye, J.M., Scholz, C.H., 1995. Relation between vein length and aperture. *J. Struct.*
702 *Geol.* 17, 423–434. doi:10.1016/0191-8141(94)00058-8

703 Vollgger, S.A., Cruden, A.R., 2016. Mapping folds and fractures in basement and cover rocks
704 using UAV photogrammetry, Cape Liptrap and Cape Paterson, Victoria, Australia. *J.*
705 *Struct. Geol.* 85, 168–187. doi:10.1016/j.jsrg.2016.02.012

706 Wilson, C.E., Aydin, A., Karimi-Fard, M., Durlofsky, L.J., Amir, S., Brodsky, E.E., Kreylos,
707 O., Kellogg, L.H., 2011. From outcrop to flow simulation: Constructing discrete fracture
708 models from a LIDAR survey. *Am. Assoc. Pet. Geol. Bull.* 95, 1883–1905.
709 doi:10.1306/03241108148

710 Wu, H.Q., Pollard, D.D., 2002. Imaging 3-D fracture networks around boreholes. *Am. Assoc.*
711 *Pet. Geol. Bull.* 86, 593–604. doi:10.1306/61EEDB52-173E-11D7-8645000102C1865D

712 *Zhang, L., Einstein, H.H., 1998. Estimating the Mean Trace Length of Rock Discontinuities.*
713 *Rock Mech. Rock Eng.* 31, 217–235. doi:10.1007/s006030050022

714 Zoback, M.D., 2007. *Reservoir Geomechanics, Reservoir Geomechanics.* Cambridge
715 University Press, Cambridge. doi:10.1017/CBO9780511586477

716

717

718 **Appendix A – Summary of aperture methods**

719 *(Sub-)linear length-aperture scaling*

720 Linear Elastic Fracture Mechanics (LEFM) predicts that aperture scales (sub-)linearly with
721 length during propagation of fractures (Atkinson, 1984; Olson, 2003; Pollard and Segall,
722 1987). Maximum opening at the centre of the fracture, d_{\max} , is defined by fracture toughness
723 K_C , the Poisson's ratio ν , Young's modulus E and fracture length L :

724
$$d_{\max} = \frac{K_C (1-\nu^2)}{E \sqrt{\frac{\pi}{8}}} \sqrt{L},$$

725 where K_C is a function of driving stress $\Delta\sigma_I$ and fracture length:

726
$$K_C = \Delta\sigma_I \sqrt{\pi L / 2}.$$

727 Discussion remains on whether aperture scales linear or sublinear with length, which has
728 large implications for apertures of relatively large fractures (Olson, 2003; Olson and Schultz,
729 2011; Scholz, 2011; Vermilye and Scholz, 1995). The impact of linear versus sublinear
730 scaling on permeability is investigated in (Bisdom et al., 2016d).

731 *Power-law scaling*

732 Outcrop studies typically find that fracture lengths follow power-law scaling distributions
733 (e.g. Bonnet et al., 2001; Bour and Davy, 1997). This, combined with the linear length-
734 aperture scaling model, implies that aperture also follows power-law scaling relations.
735 Power-law scaling of apertures is commonly observed in outcrops (Hooker et al., 2014, 2009;
736 Ortega et al., 2006), although the relation with length is rarely studied in outcrops. Instead,
737 the aperture distributions are defined independent of other geometrical or geomechanical
738 parameters, through a power-law function:

739 $F = aX^{-b},$

740 where F is the cumulative frequency, a is a density constant and b is the power-law scaling
 741 exponent (Bonnet et al., 2001). Power-law aperture distributions are the preferred method of
 742 defining aperture in industry fractured reservoir models, but they are rarely related to any
 743 other geometrical parameter. As a result, short fractures may be assigned unrealistically large
 744 apertures (Bisdom et al., 2016d).

745 *Barton-Bandis*

746 Whereas (sub-)linear length-aperture scaling predicts opening during propagation over
 747 geological times, Barton-Bandis describes present-day opening in the current stress field,
 748 assuming that fractures have irregular walls that result in conductive fractures when shearing
 749 occurs, even when fluid pressures are low (Bandis, 1980; Bandis et al., 1983; Barton, 1982;
 750 Barton and Bandis, 1980; Barton and Choubey, 1977). Mechanical aperture E_n is a function
 751 of an intrinsic initial aperture E_0 , maximum closure v_m , toughness K_{ni} and driving stress $\Delta\sigma_I$
 752 (e.g. Barton, 2014).

753
$$E_n = E_0 - \left(\frac{1}{v_m} + \frac{K_{ni}}{\Delta\sigma_I} \right)^{-1}.$$

754 Hydraulic aperture e is a function of mechanical aperture, the Joint Roughness Coefficient
 755 (JRC) and the ratio between shear (u_{geom}) and peak shear (u_{peak}) displacement (Olsson and
 756 Barton, 2001).

757
$$e = \begin{cases} \frac{E_n^2}{JRC^{2.5}} & \text{for } \frac{u_{geom}}{u_{peak}} \leq 0.75 \\ \sqrt{E_n JRC_{mob}} & \text{for } \frac{u_{geom}}{u_{peak}} \geq 1 \end{cases}.$$

758 This aperture model is strongly dependent on the local normal and shear stress acting on each
759 fracture segment, which is most accurately determined using geomechanical Finite-Element
760 models with discrete fractures (Bisdom et al., 2016b; Lei et al., 2014).

761 Alternatively, an approximation of Barton-Bandis apertures can be made without use
762 of numerical models. Using a far field stress and fracture geometry, aperture can be
763 approximated (Bisdom et al., 2016c). This model is strongly dependent on stress angle α
764 between fracture strike and σ_1 :

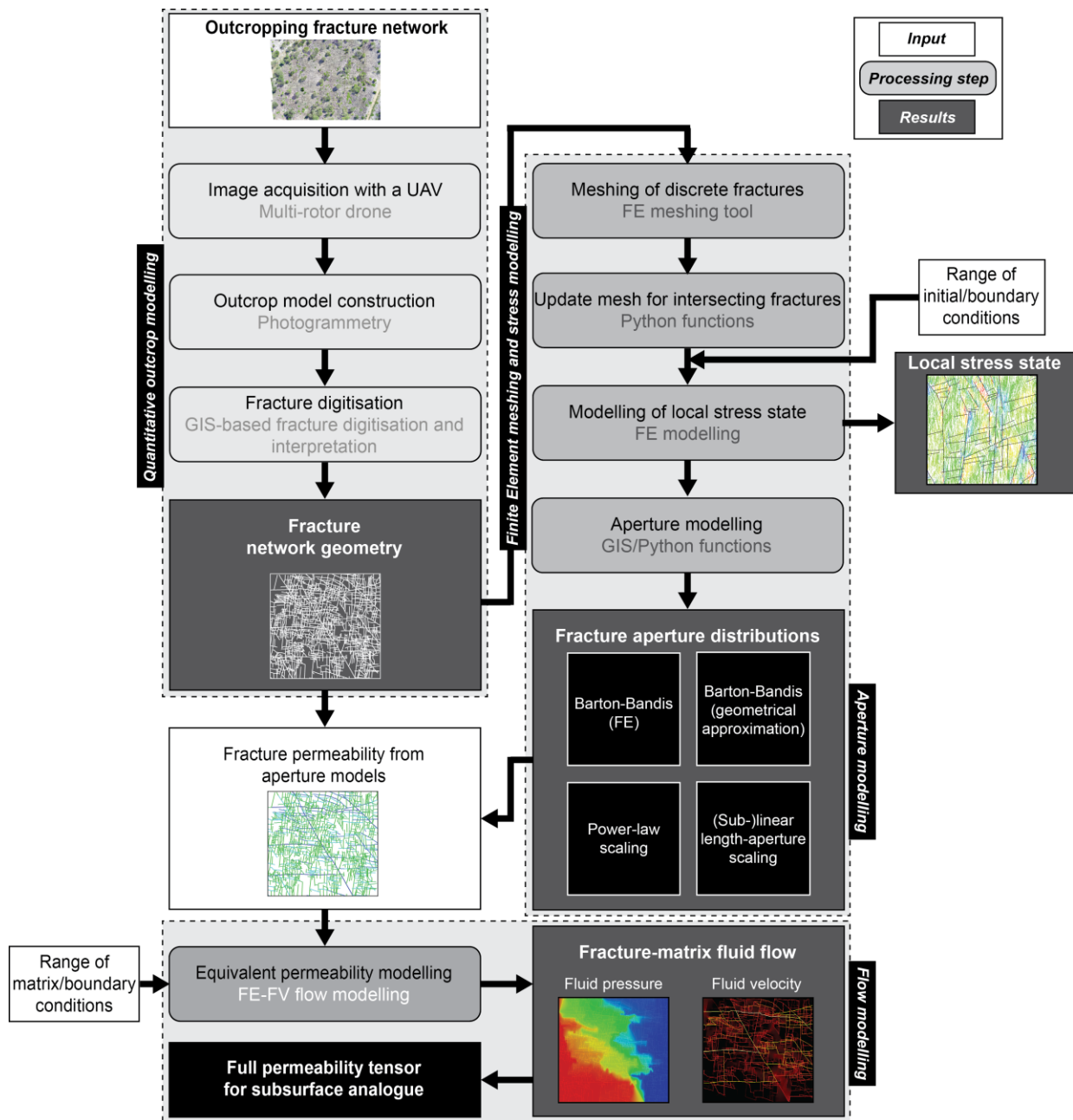
$$765 \quad \sigma_{n,angle} = 0.0054\sigma_1\alpha + 1.5186\sigma_1^{0.723} .$$

766 Normal stress is further corrected for length L and spacing S :

$$767 \quad \sigma_{n,geom} = \sigma_{n,angle} (-0.083 \ln L + 1.055) \cdot 0.996 \cdot S^{-0.008} .$$

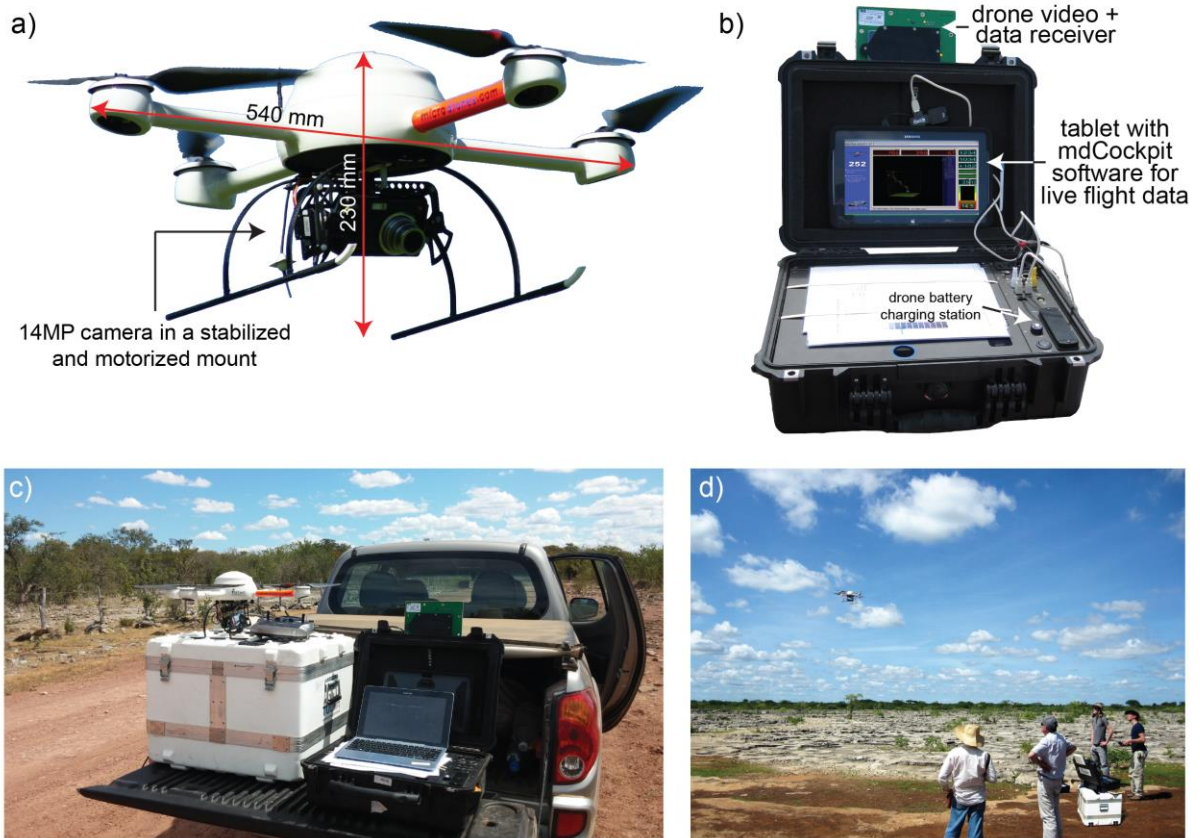
768 Shear displacement is also defined as a function of length and stress angle:

$$769 \quad u_{geom} = L \cdot \sigma_1 \cdot \alpha (-9.07 \cdot 10^{-8} \alpha + 8.1 \cdot 10^{-6}) .$$



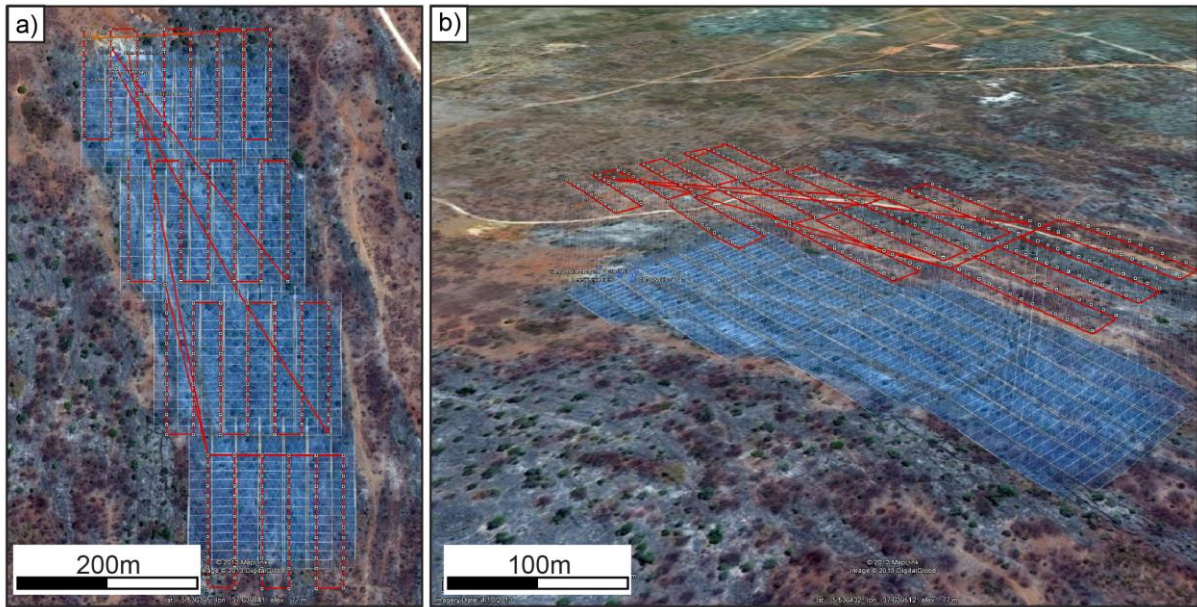
771

772 **Figure 1** Workflow for obtaining flow-based principal permeability from outcropping
 773 fracture networks that are representative of subsurface reservoir stress and pressure
 774 conditions, by taking into account the impact of stress on aperture and flow. See Appendix A
 775 for details on the aperture models.



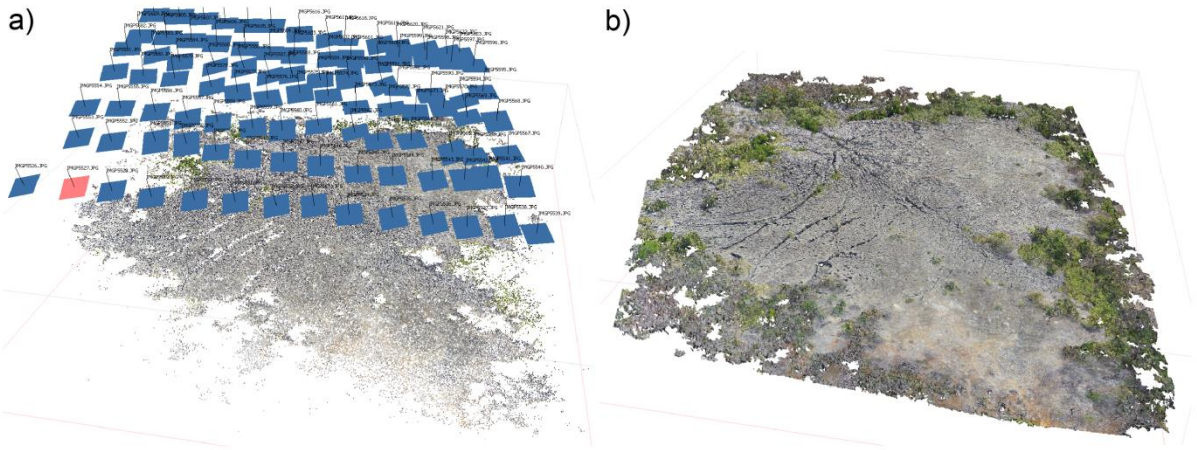
776

777 *Figure 2 Overview of the UAV equipment in the field: a) UAV (microdrones md4-200) with*
 778 *compact camera; b) Base station with receivers and tablet to receive and store flight data*
 779 *and video; c) Preparation for UAV deployment in the field. White case is the UAV transport*
 780 *case; d) Use of the UAV to image carbonate pavements.*



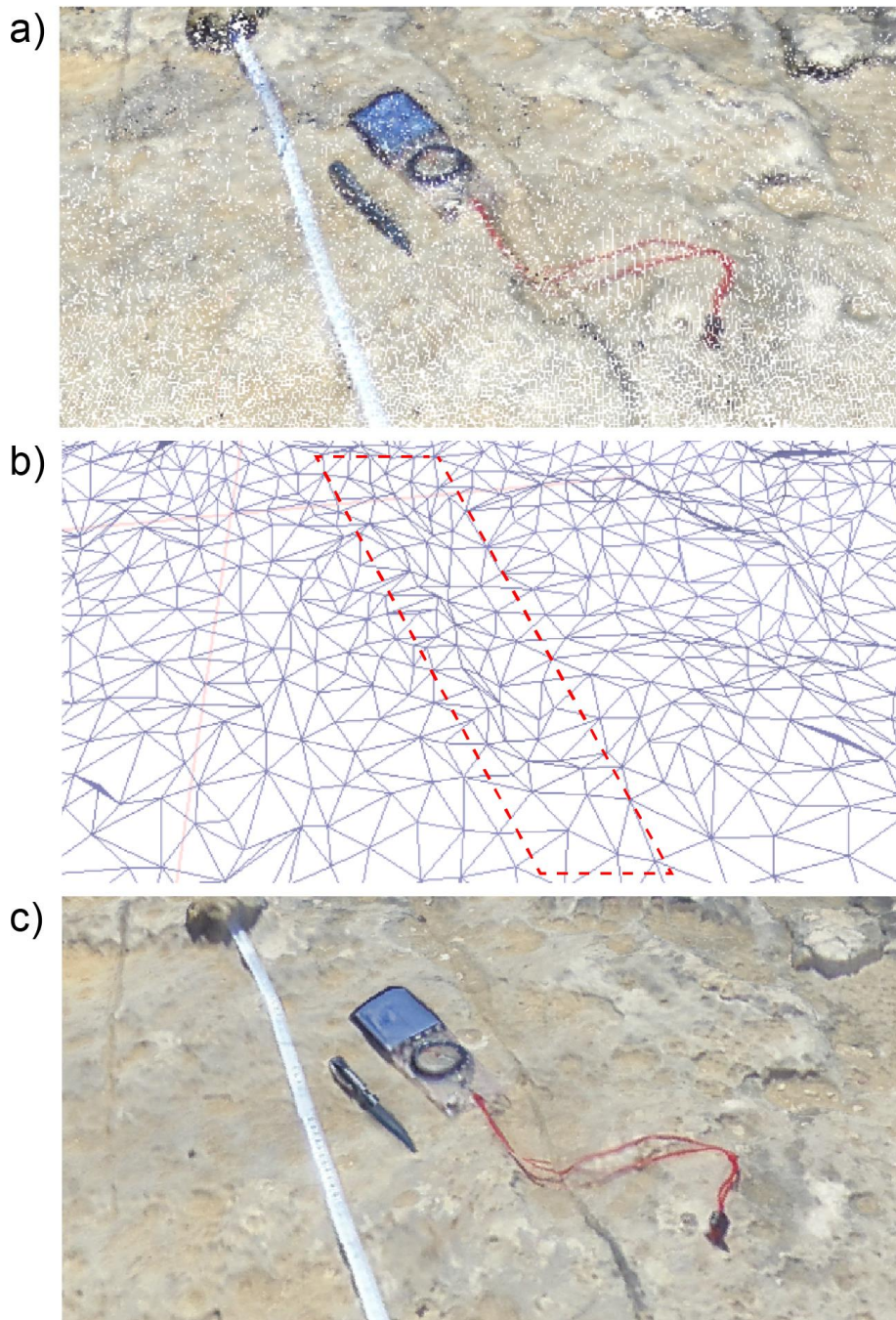
781

782 *Figure 3 Programming and visualising GNSS-steered flights: a) Top view of flight path (red)*
 783 *and imaged area (blue) in Google Earth; b) 3-D of the flight path, allowing for checking the*
 784 *programmed flight altitude with respect to ground level.*



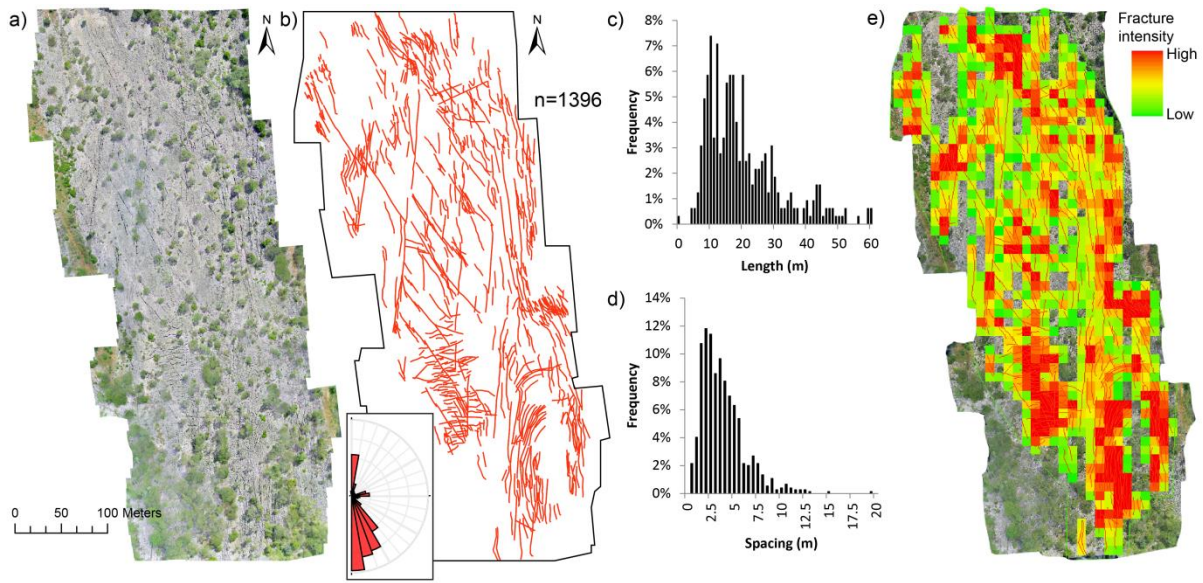
785

786 *Figure 4 Generating a 3-D outcrop model from georeferenced photographs using*
 787 *photogrammetry: a) Alignment of the images (rectangles) based on their GNSS position and*
 788 *common points extracted from the images. The image name is shown for each image (small*
 789 *texts); b) 3-D high-resolution point cloud of the outcrop.*



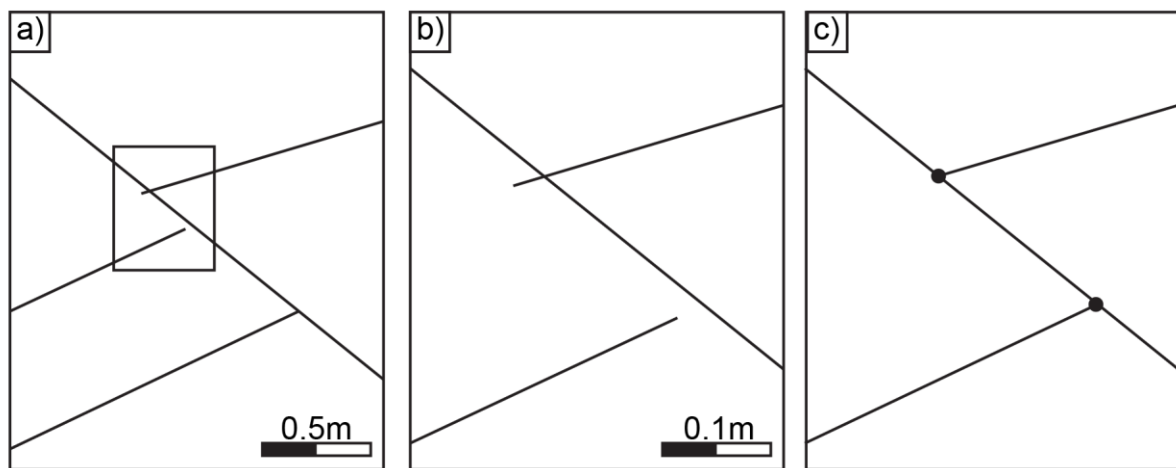
790

791 **Figure 5** Constructing a 3-D meshed surface from the point cloud: a) Detail view of the dense
792 point cloud with a resolution of 1.4×10^4 points *per* m^2 , showing a compass and pen for scale;
793 b) Triangular mesh constructed for the area from (a). The mesh has a lower resolution than
794 the point cloud, but does still indicate the main discontinuities, such as the fracture within the
795 red dashed area; c) Texture extracted from the original photographs, projected onto the
796 mesh.



797

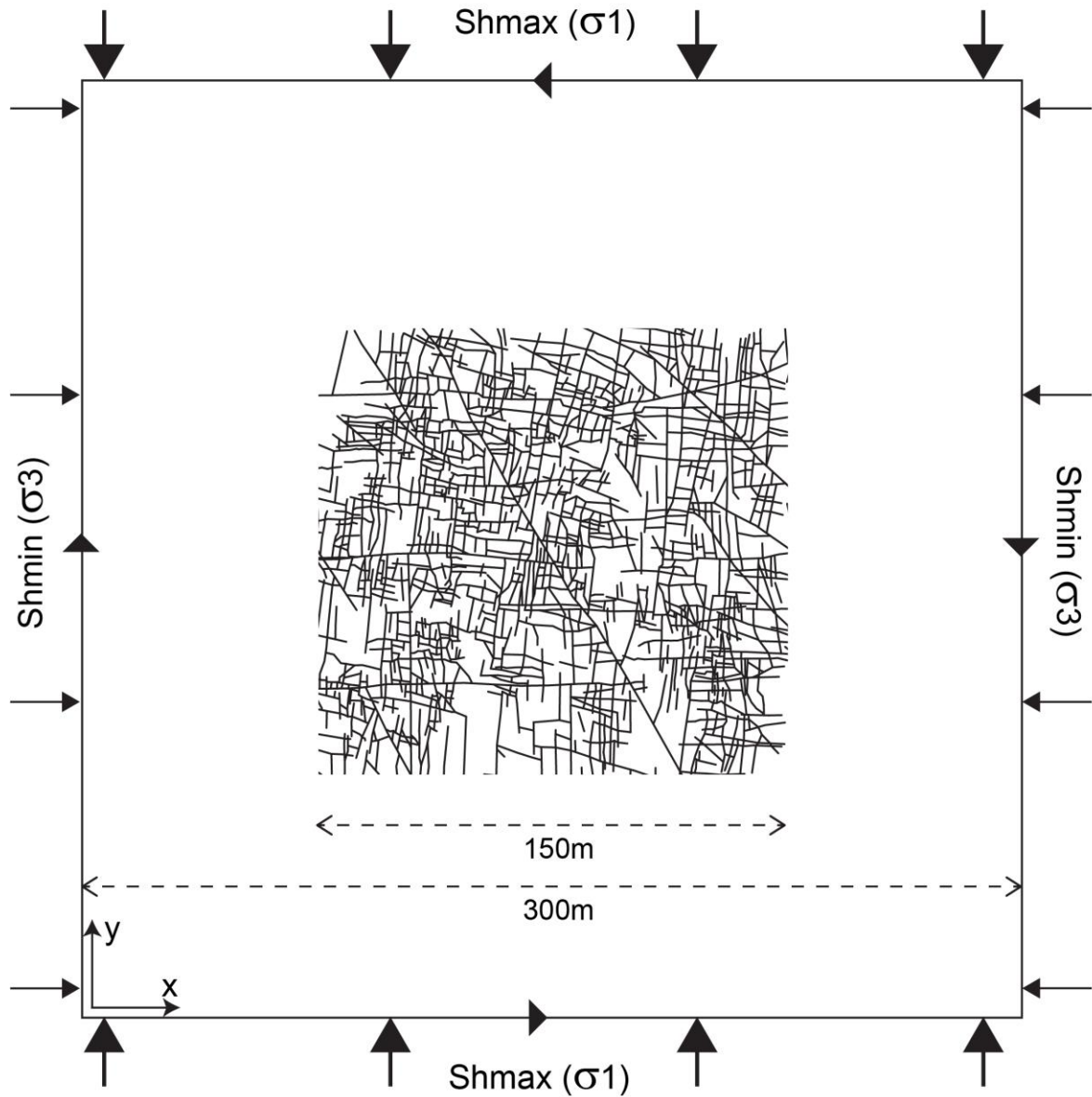
798 *Figure 6 Fracture digitisation and analysis in DigiFract using a 2-D orthomosaic of a*
 799 *carbonate pavement, constructed from 400 photographs taken from an altitude of 50 m,*
 800 *resulting in a orthomosaic resolution of 1.44 cm/px: a) The orthomosaic used for fracture*
 801 *digitisation; b) The digitised fracture network; c) Fracture length distribution; d) Fracture*
 802 *spacing distribution calculated using a box-counting method; e) Spatial fracture intensity*
 803 *calculated using box-counting.*



804

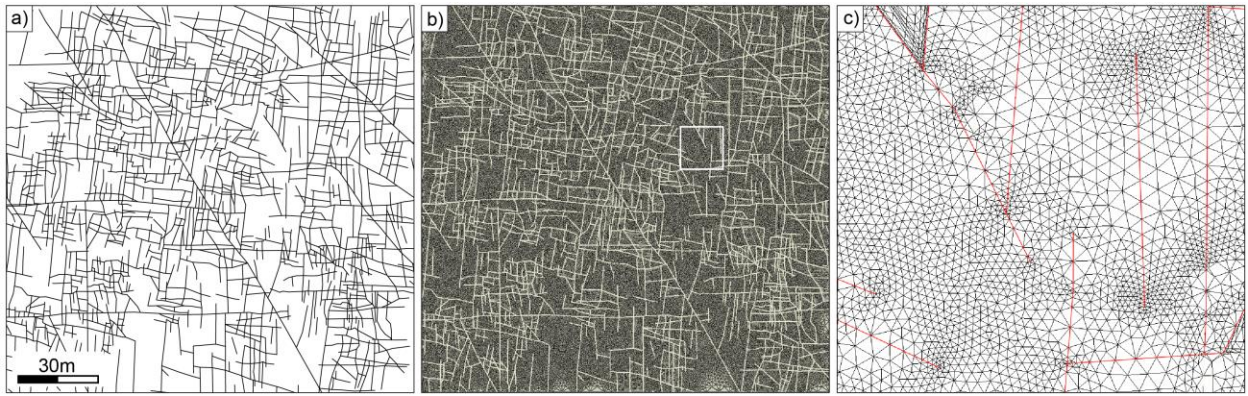
805 *Figure 7 Removal of minor gaps and overlaps to accurately represent the network topology:*
 806 *a) Three small fractures terminating against one larger fracture, with incorrect connections;*

807 b) Detail showing one overlapping segment and one segment with a gap; c) Correct fracture
808 network interpretation using snapping.



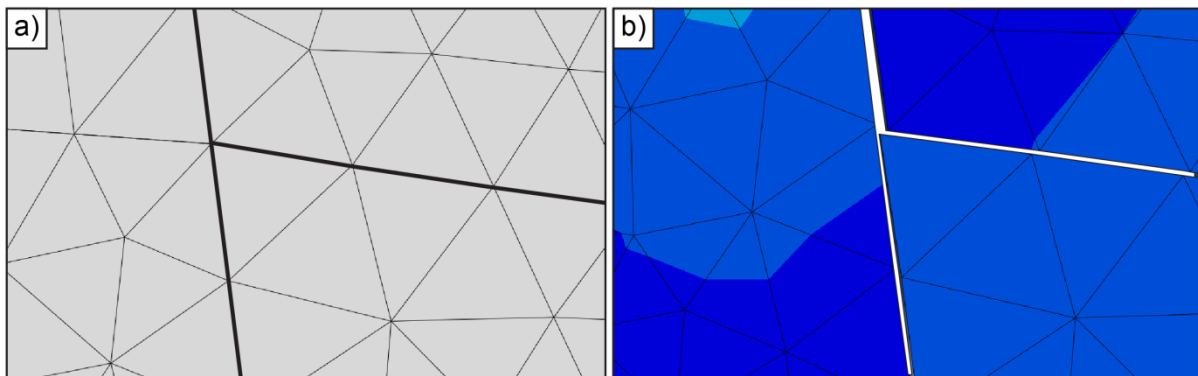
809
810 **Figure 8** Set-up of an elastic mechanical fracture network, using a $50\text{ m} \times 50\text{ m}$ fracture
811 pattern from a carbonate outcrop in central Tunisia (Bisdorn et al., 2016b). Maximum
812 horizontal stress σ_1 (30 MPa) is applied in the y-direction, resulting in a σ_3 of 10 MPa in the
813 x-direction, for a Poisson's ratio of 0.3. We apply displacement boundary conditions on the
814 centre points of each boundary to ensure symmetrical deformation.

815

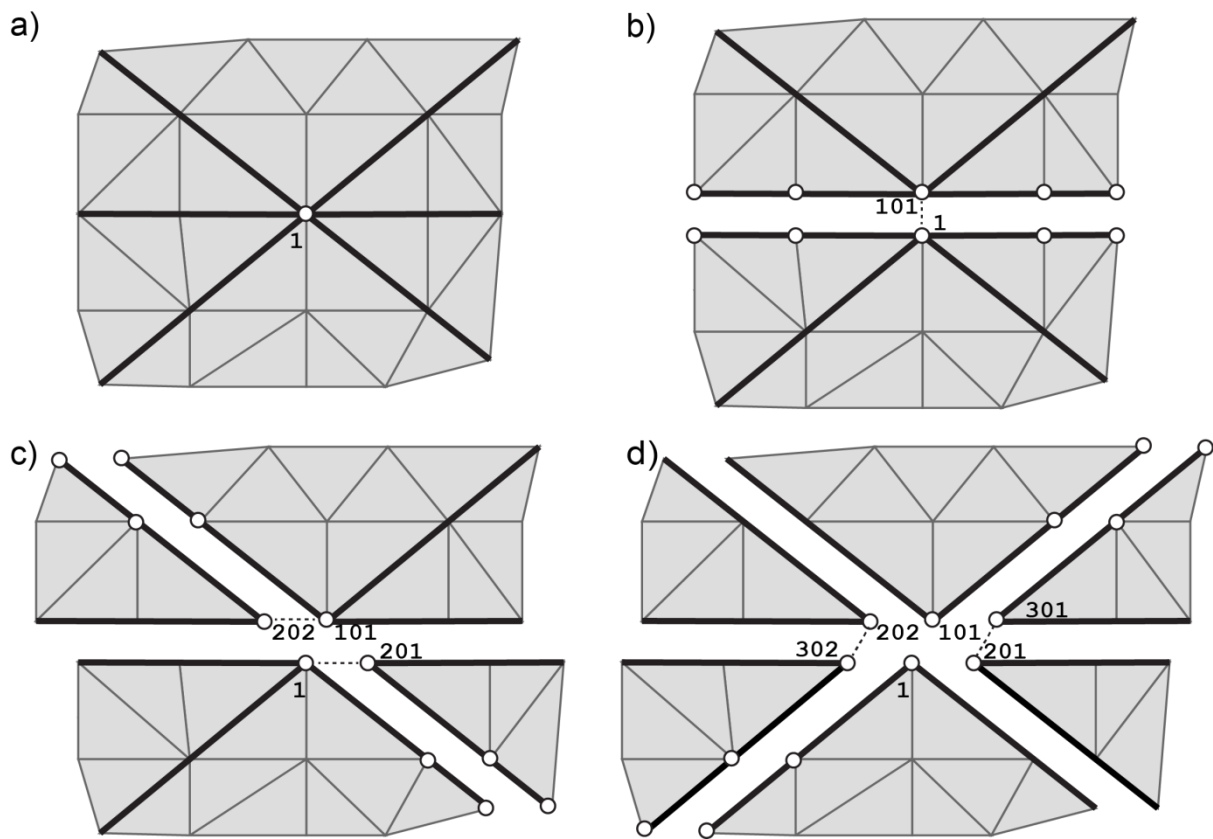


816 *Figure 9* Converting a deterministic fracture network into a triangular mesh: a) $150\text{ m} \times 142$
817 *m* section extracted from an outcropping carbonate pavement in the Potiguar basin (NE
818 Brazil); b) Meshed fracture network geometry; c) detail of the mesh showing refinement
819 around the fracture terminations and intersections (location indicated by the white square in
820 (b).

821

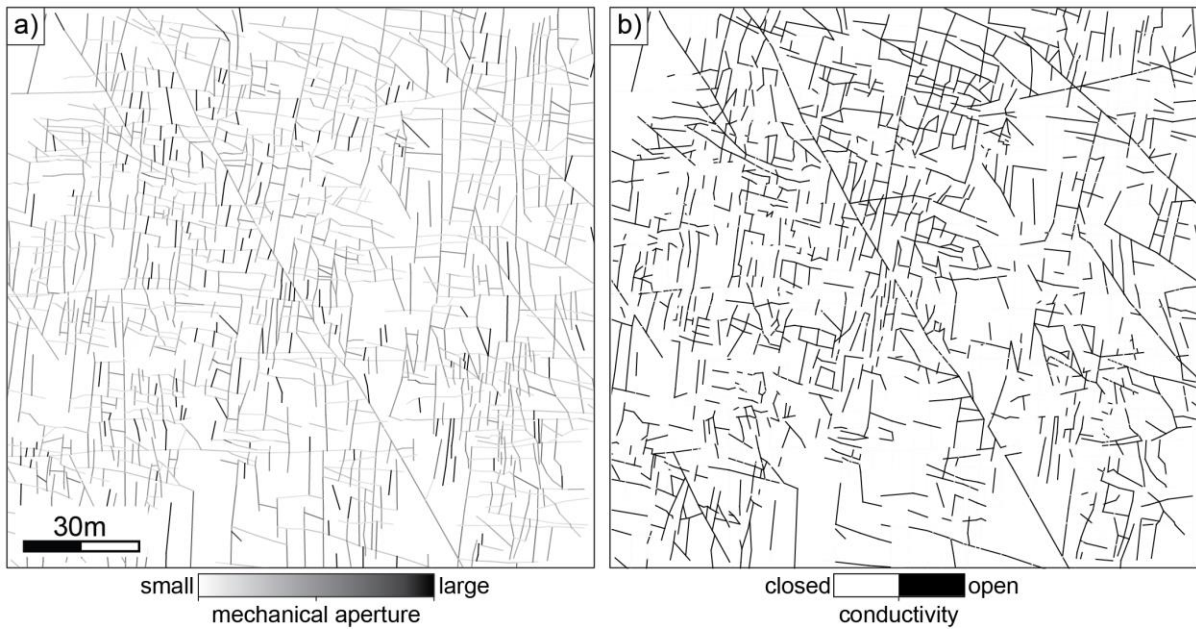


822 *Figure 10* Aperture in the FE models is modelled by representing the fractures as seams in
823 the mesh, which can open or close as a function of local stress: a) Input mesh with two
824 fractures indicated by the thick lines; b) Result after simulation, showing the stresses in the
825 mesh and the resulting fracture opening along the seams.



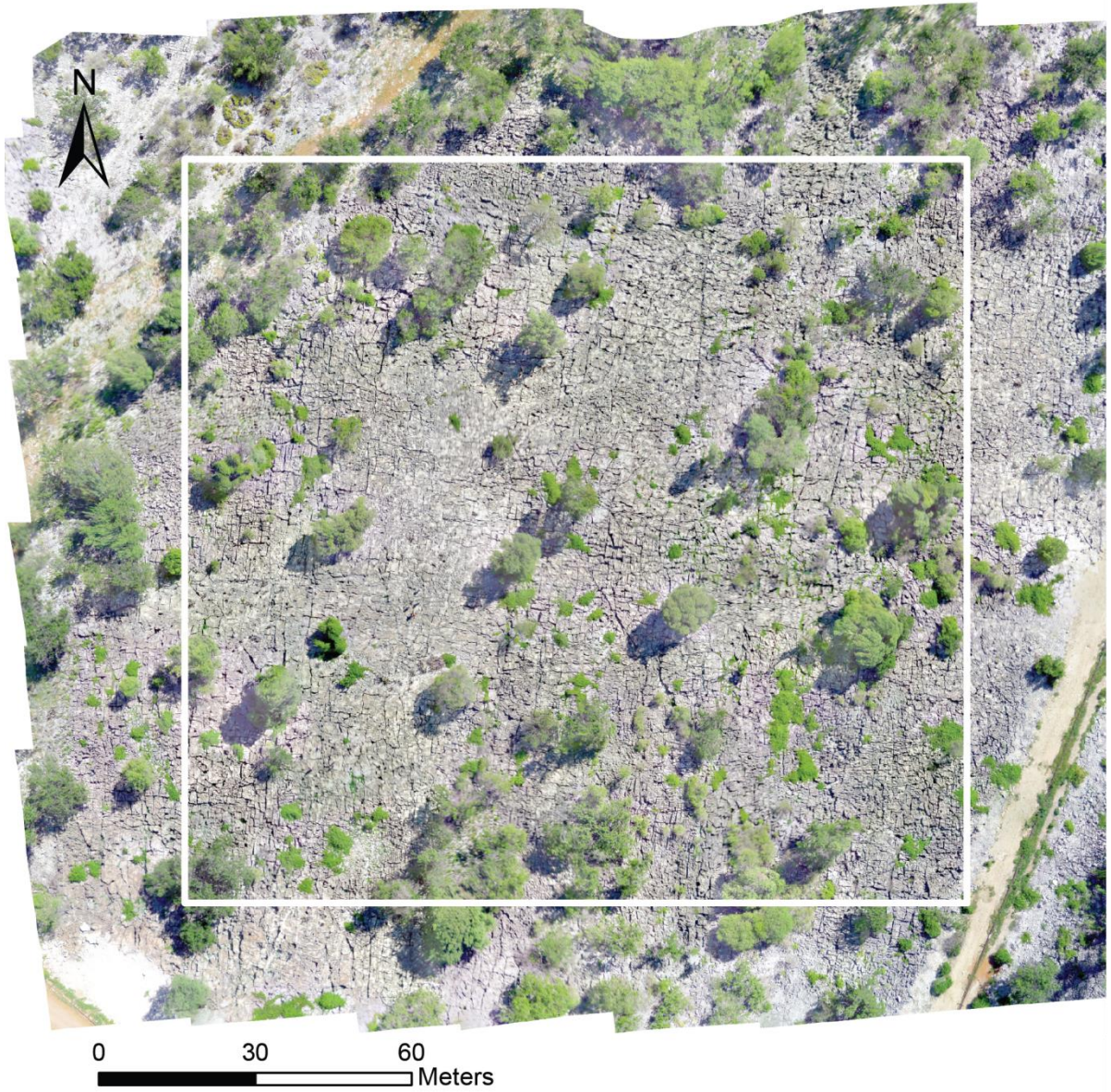
826

827 *Figure 11 Example illustrating the process of generating complex fracture intersections for*
 828 *three fractures that share a single intersection. The original node at this intersection, with*
 829 *identifier 1, is duplicated several times to generate the intersecting seams: a) Original mesh*
 830 *with fractures indicated by bold lines; b) Generating the first fracture by splitting nodes –*
 831 *node 1 is duplicated to 101; c) Second fracture requires duplication of both node 1 and 101*
 832 *(1 → 201, 101 → 202); d) The third intersecting fracture requires duplication of the last two*
 833 *nodes formed (201 → 301, 202 → 302).*



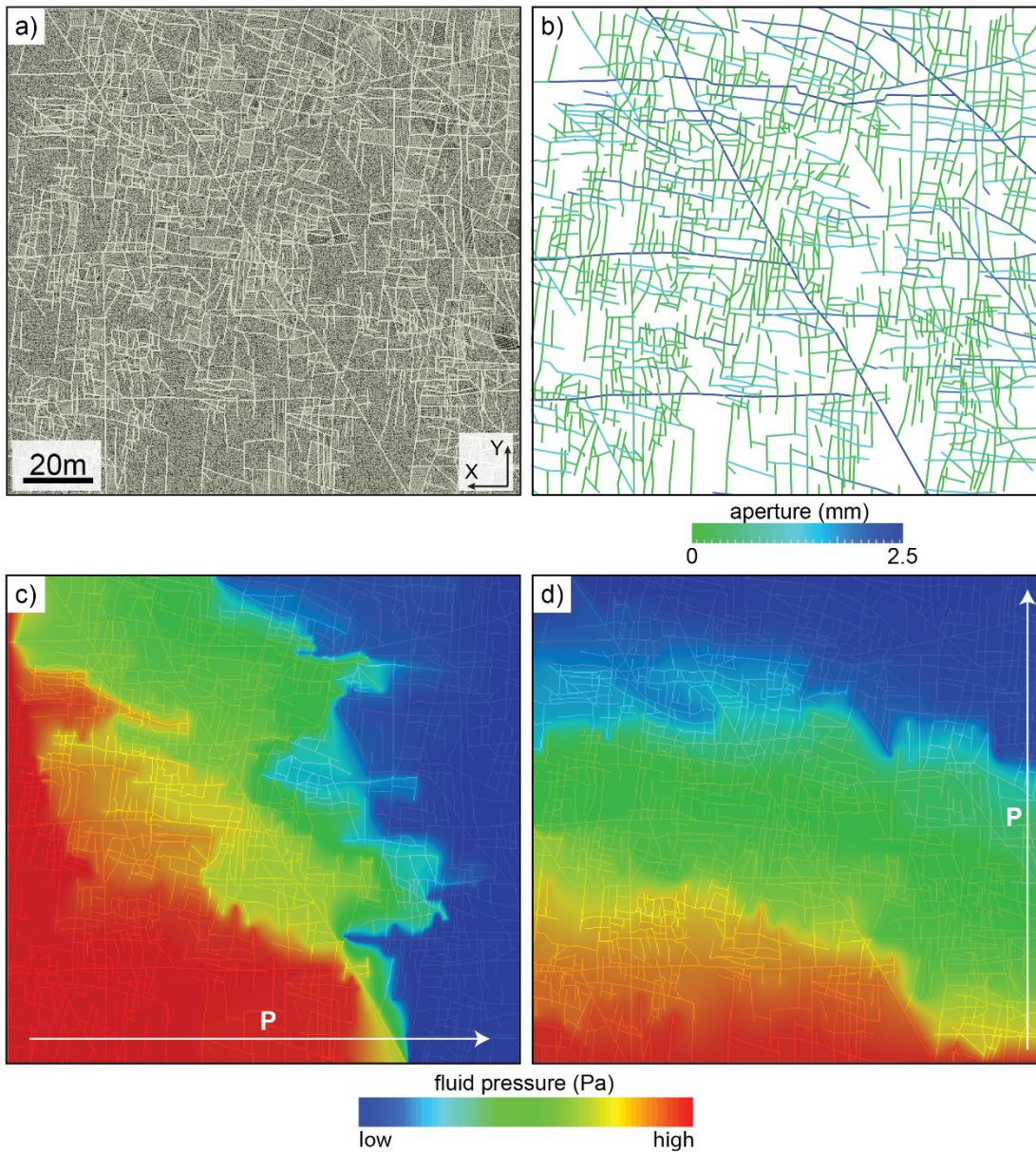
834

835 *Figure 12 Stress-induced aperture modelling: a) Mechanical aperture defined by Barton-*
 836 *Bandis, calculated from normal and shear stresses acting on each fracture segment, under a*
 837 *N-S regional σ_1 of 30 MPa and an E-W σ_3 of 10 MPa; b) Identification of hydraulically*
 838 *conductive fractures using the Barton-Bandis model, for the same stress boundary*
 839 *conditions.*



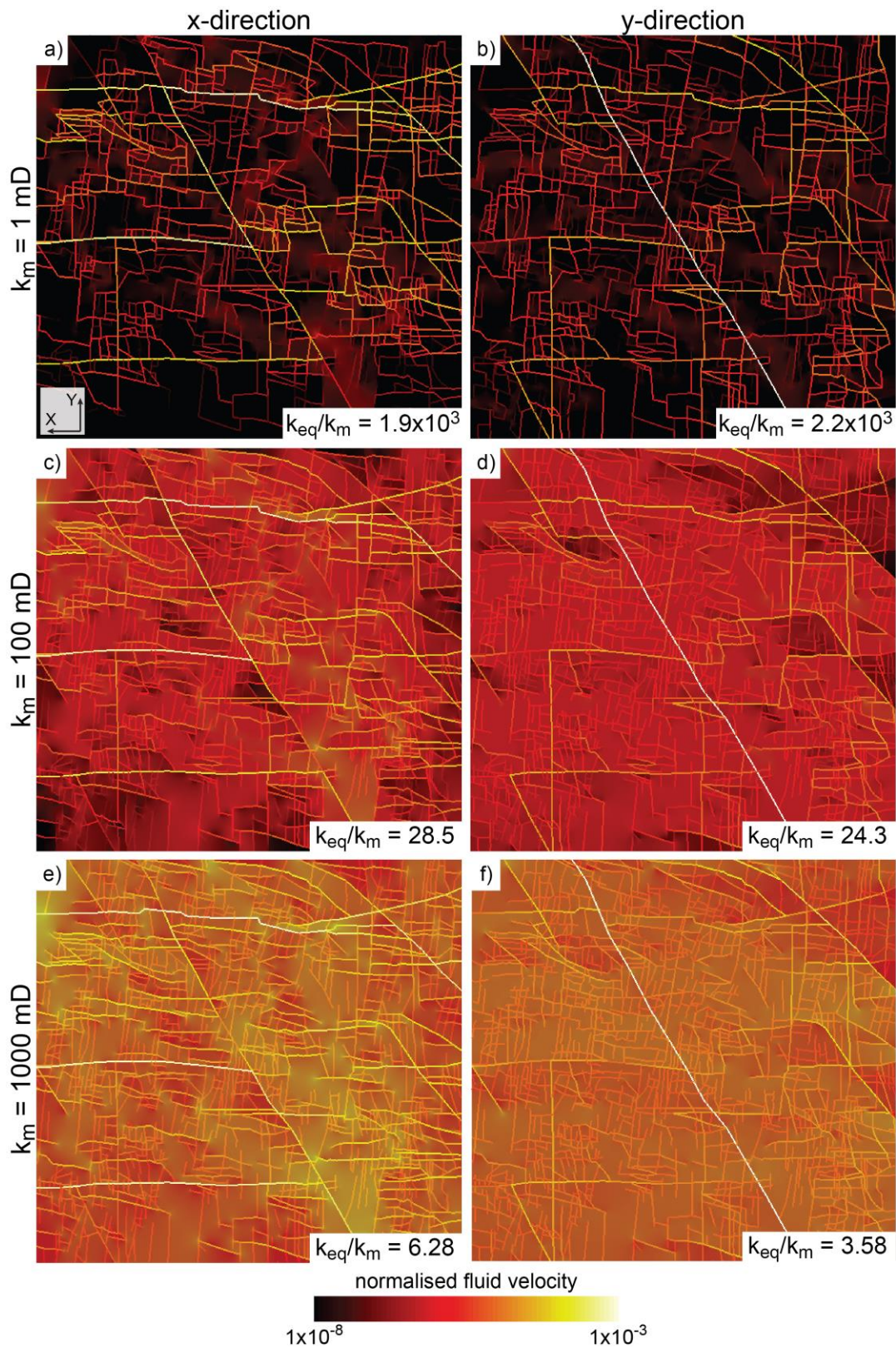
840

841 *Figure 13 High-resolution orthomosaic (1.44 cm/px resolution) of part of an outcrop in the*
842 *Potiguar basin (lat/long: -5.53092°, -37.6283°) constructed from 90 georeferenced images.*
843 *The white boundary indicates the domain that is considered for stress and flow modelling.*



844

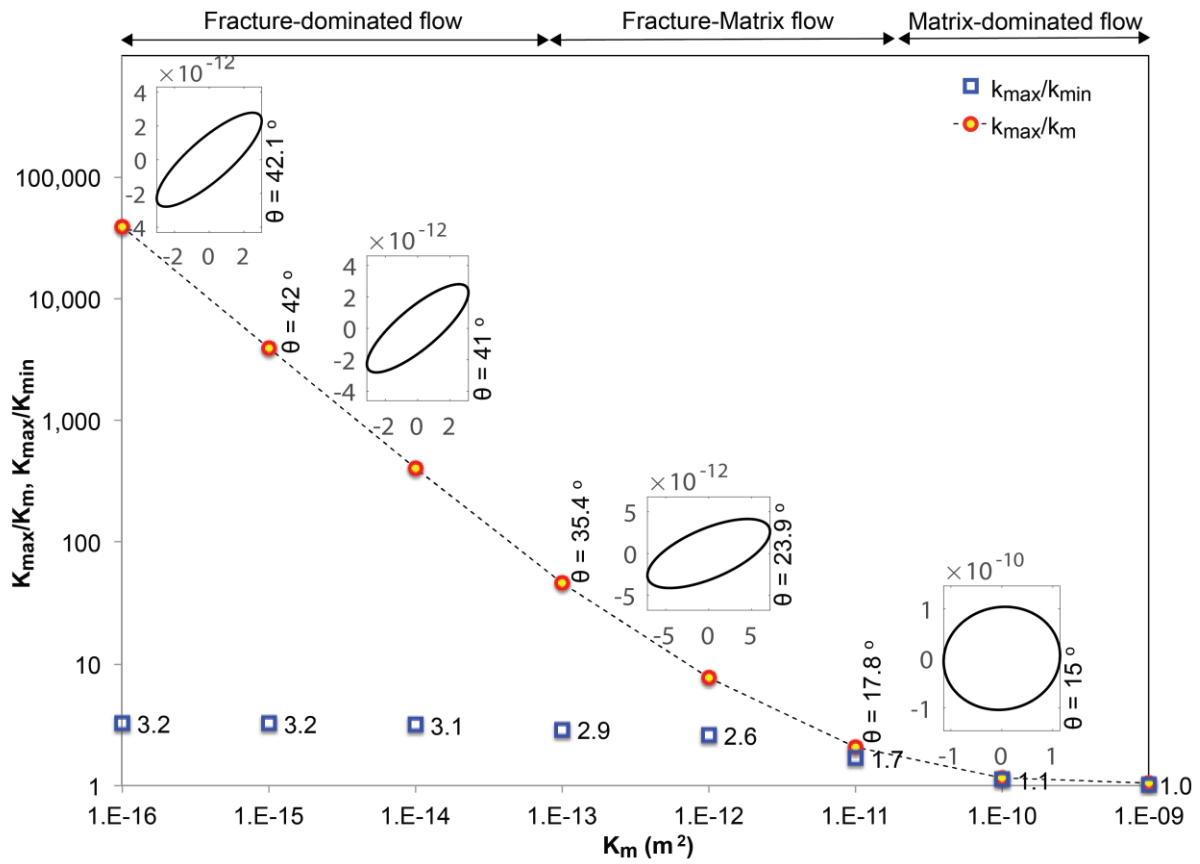
845 *Figure 14 Aperture and permeability results: a) 2-D mesh with 5.1×10^5 triangular matrix*
 846 *elements and 3.3×10^4 linear fracture elements; b) Aperture distribution derived from the*
 847 *local stress state assuming sublinear length-aperture scaling relations with a maximum*
 848 *horizontal stress oriented in the y-direction; c) **Pressure gradient** in the x-direction (indicated*
 849 *by arrow) for a 1 mD matrix permeability; d) Fluid pressure in the y-direction.*



850

851 *Figure 15 Fluid velocity magnitudes under far-field pressure gradient in the x-direction (a, c,*

852 *e) and y-direction (b, d, f) for different matrix permeabilities.*



854

855 *Figure 16 Maximum permeability versus matrix permeability for a range of matrix*
 856 *permeabilities. The direction of maximum permeability is indicated by the ellipses and θ ,*
 857 *measured from the East. The ratio between minimum and maximum permeability remains*
 858 *relatively constant except for Darcy-scale flow, where permeability is completely controlled*
 859 *by matrix flow.*